Geol. Mag. **156** (*4*), *2019, pp. 639–658* © *Cambridge University Press 2018*
doi:10.1017/S001675681700111X

Mineralization of Luziyuan Pb–Zn skarn deposit, Baoshan, Yunnan Province, SW China: evidence from petrography, fluid inclusions and stable isotopes

YU-LONG YANG*‡§, LIN YE*†, TAN BAO*||, WEI GAO*|| & ZHEN-LI LI*||

*State Key Laboratory of Ore Deposit Geochemistry, Institute of Geochemistry, Chinese Academy of Sciences, Guiyang 550002, China
‡School of Earth Sciences and Engineering, Nanjing University, Nanjing 210093, China
§College of Earth Sciences, Chengdu University of Technology, Chengdu 610059, China
||Graduate School of Chinese Academy of Sciences, Beijing 100039, China

(*Received* 26 June 2016; *accepted* 27 November 2017; *first published online* 18 January 2018)

Abstract – The Luziyuan Pb–Zn skarn deposit, located in the Baoshan–Narong–Dongzhi block metallogenic belt in SW China, is hosted by marble and slate in the upper Cambrian Shahechang Formation. Three skarn zones have been identified from the surface (1495 m above sea level (asl)) to a depth of 1220 m asl: zone 1 consists of chlorite–actinolite–calcite–quartz, zone 2 of rhodonite–actinolite–fluorite–quartz–calcite, and zone 3 contains garnet–rhodonite–actinolite–fluorite–quartz–calcite. The deposit formed in four distinct mineralization stages: an early anhydrous skarn (garnet, rhodonite and bustamite) stage (Stage 1), a hydrous skarn (actinolite and chlorite) stage (Stage 2), an early quartz (coarse barren quartz veins) stage (Stage 3) and a late sulphide-forming (fine sulphide-bearing quartz veins) stage (Stage 4). The Stage 1 skarn-forming fluid temperature was at least 500 °C according to the geothermometer with rhodonite/bustamite trace elements measured by laser ablation – inductively coupled plasma – mass spectrometry (LA-ICP-MS). A decrease in ore fluid temperatures with time is consistent with the decreases in the $\delta^{18}O_{fluid}$ and δD_{fluid} values from Stage 3 to 4. This trend suggests that the ore fluid was mainly derived from magmatic water and mixed with large amounts of meteoric water during mineralization. The $\delta^{34}S$ values of Stage 4 chalcopyrite, sphalerite and galena are similar to those of an Ordovician gypsum layer, and together with the high-salinity fluids in Stage 4 indicate the dissolution of evaporites in the Luziyuan region. Overall, the results of this study suggest that the Luziyuan deposit is a distal Pb–Zn skarn deposit that formed in response to multi-stage alteration associated with a combination of magmatic water and meteoric water.

Keywords: rhodonite, fluid inclusion, stable isotopes, ore-forming fluid, Luziyuan distal Pb–Zn skarn deposit, southwest China.

1. Introduction

Many Fe and Cu skarn deposits occur at or near contact zones between carbonate rocks and igneous intrusions (Meinert, Dipple & Nicolescu, 2005). However, some skarn-type Pb–Zn–Ag deposits are hosted in carbonate rocks and are relatively far from any direct influence of an intrusive mass. These skarn deposits are characterized by manganese skarn minerals (rhodonite, bustamite and vogtite) and are defined as distal skarn-type Pb–Zn deposits (Meinert, 1987; Meinert, Dipple & Nicolescu, 2005).

There are three predominant mechanisms responsible for the formation of skarn deposits: (1) fluid phase separation; (2) mixing of fluids; and (3) interaction between fluids and wallrock (Ahmad & Arthur, 1980; Wilkinson, 2001; Peter *et al.* 2004). Many workers (González-Partida & Camprubí, 2006; Bertelli *et al.* 2009; Kamvong & Zaw, 2009; Mollai, Sharma & Pe-Piper, 2009; Canet *et al.* 2011; Palinkas *et al.* 2013; Yang *et al.* 2013) have studied the origin of ore-forming fluids and the depositional mechanisms of some Pb–Zn skarn deposits based on the skarn mineral compositions (e.g. garnet and diopside), isotopic compositions (C, H, O and S isotopes) of minerals, such as hedenbergite, quartz, calcite and sulphides, and fluid inclusion geochemistry. These studies have shown that sulphide mineralization can occur during different ore-forming processes, including fluid–rock interaction (Bertelli *et al.* 2009), fluid boiling (Mollai, Sharma & Pe-Piper, 2009; Canet *et al.* 2011) and fluid mixing between magmatic and meteoric fluids (González-Partida & Camprubí, 2006; Kamvong & Zaw, 2009; Palinkas *et al.* 2013; Yang *et al.* 2013). Therefore, the origin of the fluid and precipitation mechanisms responsible for the formation of the sulphide mineralization are the subject of considerable debate.

The Luziyuan skarn-type Pb–Zn deposit was discovered in 2006 in the Baoshan–Narong–Dongzhi block metallogenic belt (BND belt) in Yunnan Province, China. The current reserves are estimated at 1.9 Mt of Pb + Zn metal in ores with a Pb grade of

†Author for correspondence: yelin@vip.gyig.ac.cn

https://doi.org/10.1017/S001675681700111X Published online by Cambridge University Press

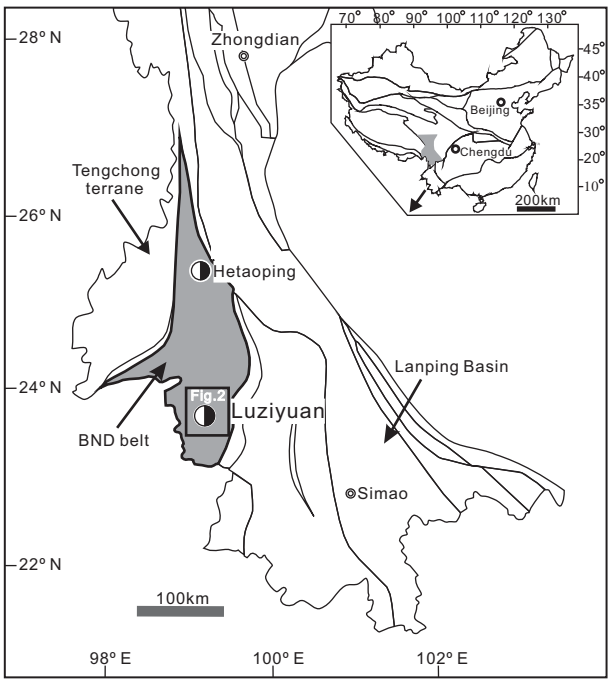

Figure 1. Regional geological setting of the Luziyuan skarn-type Pb–Zn deposit within the Baoshan–Narong–Dongzhi (BND) belt (adapted from Ye *et al.* 2011*a*). The small box shown is expanded in Figure 2.

0.6–5.2 % and a Zn grade of 1.6–13.2 %. The geological features of the deposit have been well characterized by many researchers because of its local and regional economic importance in the BND belt (Zhao, Lu & Xie, 2002; Dong & Chen, 2007; Yang & Luo, 2011; Ye *et al.* 2011*a*; Ye, Yang & Bao, 2011*b*; Yang *et al.* 2012; Cang, Deng & Wang, 2013; Deng, Li & Wen, 2013; Lin *et al.* 2013; Ye, Bao & Yang, 2013). However, to date, only two studies (published in Chinese only) have examined the fluid inclusions and ore deposit genesis (Xia, Chen & Lu, 2005; Cang, Deng & Wang, 2013).

The present study provides fluid inclusion and stable isotope data obtained from both ore and gangue minerals from the Luziyuan deposit. The purpose of this paper is to provide a better understanding of the origin of the ore-forming fluid and to discuss the general mechanisms that control the formation of the skarn-type deposit at Luziyuan.

2. Geological setting

2.a. Regional geology

The Luziyuan skarn-type Pb–Zn deposit is hosted in the BND belt of the Dian-Tai-Ma metallogenic province (Fig. 1). The BND belt is bounded to the west by the Nujiang abyssal fault and to the east by the Kejie fault. It is the main metallogenic belt between the Tengchong terrane and Changning–Menglian suture zones. This belt hosts two similar skarn-type deposits (Fig. 1), the Hetaoping and the Jinchang skarn-type Pb–Zn deposits, both of which have been discussed in several previous studies (Chen, Lu & Xia, 2005; Zhu, Han & Xue, 2006; Xue, Han & Yang, 2008; Chen, Huang & Lu, 2009; Han, 2010; Gao *et al.* 2011; Xue *et al.* 2011; Yang *et al.* 2013).

There is evidence of minor intermediate to felsic igneous activity in the Luziyuan ore district, of which the Muchang alkaline granite is the most conspicuous example. The Muchang granite is characterized by high FeO_t/MgO and 10000*Ga/Al ratios with A-type granite affinities (Ye *et al.* 2010). Dating of zircons from the intrusion indicates an age of 266 ± 5.4 Ma (U–Pb, laser ablation – inductively coupled plasma – mass spectrometry (LA-ICP-MS)) (Ye *et al.* 2010). However, the Luziyuan Pb–Zn mineralization (which has a Sm–Nd age of 183 ± 2.3 Ma, Yanshanian; Yang, 2013) was not associated with the Muchang intrusion. Additionally, an unexposed intermediate-acidic intrusion in the Luziyuan mining area is considered to be related to the Muchang intrusion and a product of mid-Permian igneous activity (Ye *et al.* 2010). The gravity low anomaly and negative aeromagnetic anomaly were found in the Luziyuan area and have been interpreted to be linked to the concealed intrusion (Li & Mo, 2001; Zhao, Lu & Xie, 2002; Dong & Chen, 2007).

2.b. Geology of the Luziyuan deposit

The Luziyuan skarn-type Pb–Zn deposit consists of three orebodies (I, II, III) from the northwest to the southeast (Fig. 2a). Field surveys at 1220 m, 1265 m and 1495 m above sea level (asl) of the second orebody (II) indicate that the deposit has a predominantly stratiform architecture, with parallel sedimentary layers (Fig. 2b). The deposit is hosted by upper Cambrian rocks, including marble and slate of the Shahechang Formation, and is relatively far from the concealed intermediate-acidic intrusion, a feature shared by other distal skarn-type Pb–Zn deposits (Einaudi, Meinert & Newberry, 1981; Shimizu & Ilyama, 1982; Yun & Einaudi, 1982; Meinert, 1987; Meinert *et al.* 2003; Williams-Jones *et al.* 2010; Palinkas *et al.* 2013). The country rock was subjected to widespread skarn alteration, and field surveys conducted in this study showed that, based on variations in the mineral assemblage, there were three different alteration zones at different depths, as follows (Figs 2b, 3): (1) an actinolite zone (1495 m asl) – chlorite–actinolite–calcite–quartz; (2) a rhodonite zone (1265 m asl) – rhodonite–actinolite–fluorite–quartz–calcite; and (3) a garnet zone (1220 m asl) – garnet–rhodonite–actinolite–fluorite–quartz–calcite.

The distinguishing criterion of the zone 1 assemblage is actinolite–chlorite, which is abundant in the upper part of the skarn system (1495 m), where it forms veins several centimetres to several metres wide around the No. II orebody (Fig. 3a). Sulphide mineralization (sphalerite, galena and chalcopyrite) occurs as fine-grained veins in zone 1 (Fig. 3a) and cuts the early coarse-grained barren quartz veins (Fig. 3b). The zone 2 assemblage is found at a depth of 1265 m and

https://doi.org/10.1017/S001675681700111X Published online by Cambridge University Press

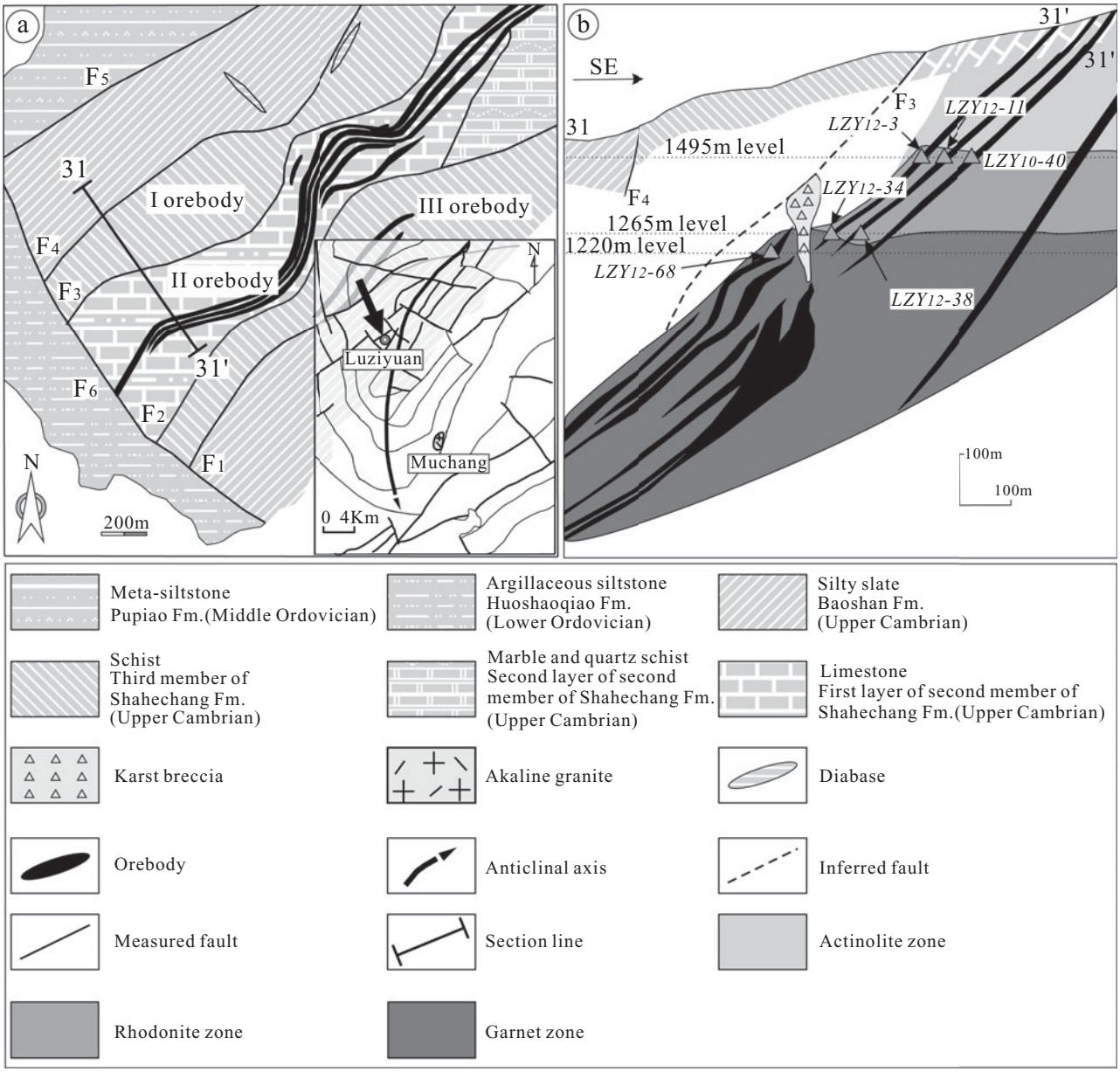

Figure 2. (a) Geological map of the Luziyuan deposit and (b) representative cross-section A–B through the deposit, showing the geometry of the orebodies, vertical skarn zonation and the location of samples collected for this study. The Huoshaoqiao Formation comprises argillaceous siltstone; the Pupiao Formation comprises meta-siltstone with intercalated meta-quartz–arenite; the Baoshan Formation comprises silty slate with intercalated argillaceous limestone; the third Member of the Shahechang Formation comprises schist with intercalated marble; the first layer of the second Member of the Shahechang Formation comprises limestone with minor siltstone, and the second layer comprises marble and quartz schist (redrawn after Lü, Deng & Hu, 2013).

is based on the occurrence of rhodonite, which forms a *c*. 50 m wide zone around the No. II orebody, thereby constituting the central part of the skarn system. Moving away from the orebody, the skarn zones occur in the following sequence: rhodonite–actinolite to quartz veins to marble (Fig. 3c). It is evident that the rhodonite in the zone 2 assemblage was replaced by actinolite (Fig. 3d). At a depth of 1220 m, pale green garnets, which are considered indicative of the zone 3 assemblage, are abundant (Fig. 3e). The zone 3 assemblage is typically *c*. 5 m wide, and the garnet–rhodonite assemblage was also replaced by the actinolite and coarse-grained barren quartz veins that are characteristic of the zone 1 assemblage (Fig. 3f). Several fine-grained sulphide-bearing quartz and calcite veins also cut across the garnet–rhodonite skarn at 1220 m.

2.c. Paragenetic relationship between skarn and ore minerals

Skarn alteration is the main form of alteration throughout the BND belt district (Fig. 3) and is represented by anhydrous (garnet, rhodonite and bustamite) and hydrous (actinolite and chlorite) skarn minerals. The ore mineral assemblage is predominantly sphalerite–galena–chalcopyrite–quartz–calcite with distinct zoning: garnet to rhodonite–bustamite,

https://doi.org/10.1017/S001675681700111X Published online by Cambridge University Press

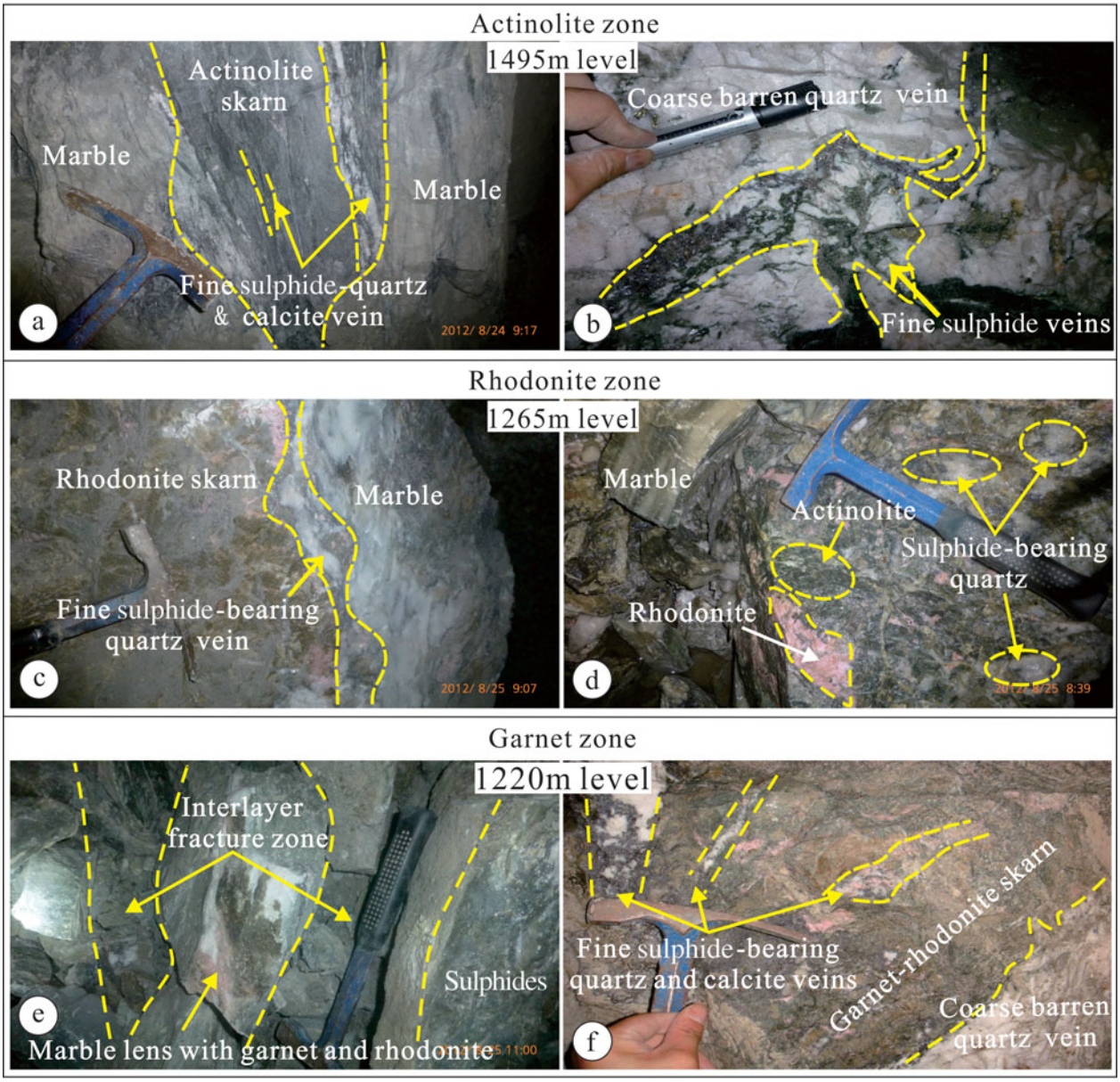

Figure 3. (Colour online) Photographs of Pb–Zn mineralization, skarnification and quartz veins from 1495 m, 1265 m and 1220 m asl in the Luziyuan orebody. (a) The 1495 m level shows replacement of carbonate host rocks by actinolite skarn and fine sulphides, quartz and calcite. (b) Coarse barren quartz vein cut by fine sulphide vein. (c) The 1265 m level shows a mineralized quartz vein with skarn replacement from the front towards the marble host rock. (d) Rhodonite relics replaced by actinolite, which was in turn replaced by sulphide-bearing quartz. (e) The 1220 m level shows a marble lens with rhodonite and actinolite in the interlayer fracture zone. (f) Garnet–rhodonite skarn cut by several fine sulphide-bearing quartz and calcite veins, replaced by coarse barren quartz veins.

followed by sphalerite–galena–chalcopyrite–quartz–calcite actinolite–chlorite, and then marble (Fig. 3c).

Petrographic studies have demonstrated that anhydrous skarn minerals (garnet, rhodonite and bustamite) are partly replaced by hydrous skarn minerals (actinolite and chlorite). In addition, the coarse-grained barren quartz veins replaced garnet–rhodonite–bustamite–actinolite skarn, and fine-grained sulphide-bearing quartz and calcite veins cut coarse-grained barren quartz veins and garnet–rhodonite–bustamite–actinolite skarn. The following vein paragenesis is determined in the ore district based on cross-cutting relationships: (1) garnet–rhodonite–bustamite–actinolite skarn (Fig. 3c, d, f); (2) coarse-grained barren veins (Fig. 3b, f); and (3) fine-grained sulphide-bearing quartz and calcite veins (Fig. 3a, e).

The following paragenetic stages of ore and gangue mineral formation have been determined from field and petrographic evidence. The anhydrous skarn-forming stage (Stage 1) (mainly rhodonite) was followed by hydrous skarn minerals (mainly actinolite) (Stage 2) and then by the early quartz stage (Stage 3), represented by the coarse barren quartz veins. Stage 4 is represented by the formation of sulphides (galena, sphalerite and minor chalcopyrite), quartz and calcite. Stages 3 and 4 are the main focus of this study. Figure 4

https://doi.org/10.1017/S001675681700111X Published online by Cambridge University Press

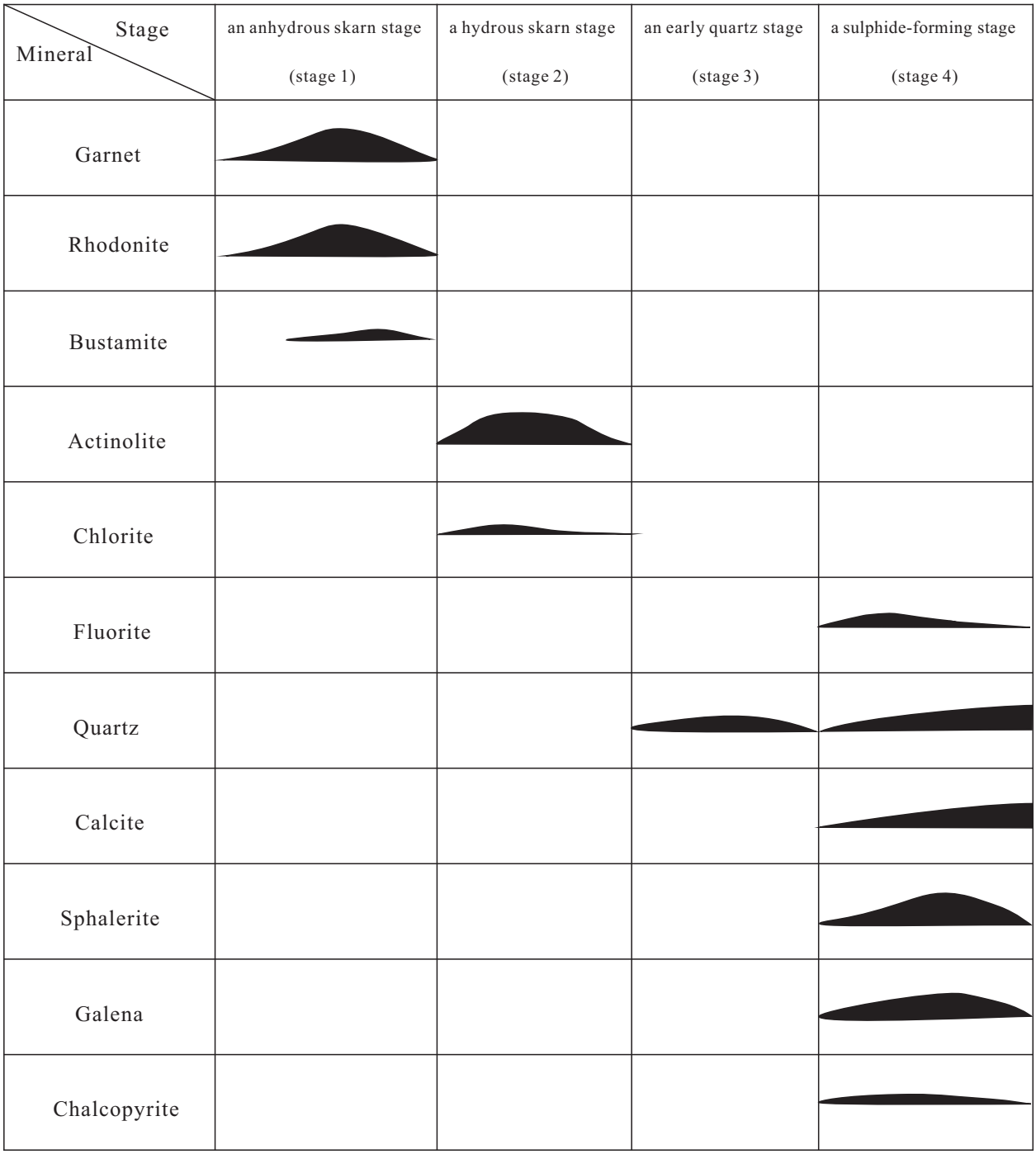

Figure 4. Generalized paragenetic sequence for skarn minerals and sulphides at the Luziyuan deposit.

illustrates a simplified paragenetic sequence for the skarn mineral assemblages and ore sulphides within the Luziyuan deposit.

3. Materials and methods

To study the Stage 1 and Stage 2 skarn minerals, two samples (LZY_{12}-34 and LZY_{12}-3) were selected. Sample LZY_{12}-34 represents the textural relationship between rhodonite and actinolite, and sample LZY_{12}-3 represents the textural relationship between actinolite and the sulphides.

To study the fluid inclusions associated with Stages 3 and 4, seven samples of the ore assemblages were gathered from three different levels (1495 m, 1265 m and 1220 m) of the No. II orebody. These samples represent two stages (3 and 4), i.e. the coarse-grained barren veins and fine-grained sulphide-bearing quartz and calcite veins.

Five samples of the Stage 3 quartz samples in the No. II orebody and five samples of the quartz, calcite and sphalerite from the Stage 4 (sulphide-forming stage) minerals were obtained for H–O isotope analyses. From these samples, it was possible to

https://doi.org/10.1017/S001675681700111X Published online by Cambridge University Press

characterize the origin of mineralizing fluid in Stages 3 and 4. In addition, 38 sulphur isotope analyses were carried out on 35 samples of sulphide ore and 3 gypsum samples of country rock from the No. II orebody. Some sample locations are shown in Figure 2b.

3.a. Mineral chemistry analysis

Mineral chemistry analyses of skarn minerals from Stages 1 and 2 were determined by a Coherent GeoLasPro 193 nm Laser Ablation system coupled with an Agilent 7700× ICP–MS at the State Key Laboratory of Ore Deposit Geochemistry, Institute of Geochemistry, Chinese Academy of Sciences, Guiyang, China. Helium was applied as a carrier gas, and argon was used as the make-up gas and mixed with the carrier gas via a T-connector before entering the ICP. The working parameters of the laser instrument were as follows: laser beam (32 um in diameter), repetition rate of 4 Hz, and energy density of 1–45 J cm^{-2}. The acquisition of data during each analysis took 60 s (20 s on background; 40 s on signal). Major contents were calibrated against multiple-standards (GSE-1G, CGSG-1 and CGSG-2). Every ten sample analyses were followed by one analysis of GSE-1G as a quality control to correct the time-dependent drift of sensitivity and mass discrimination. Detailed analytical and data-processing methodology is described by Liu *et al*. (2008). The raw ICP-MS data were treated offline using the ICPMSDataCal software (Liu *et al*. 2008).

3.b. Microthermometry analysis

The microthermometry investigation of fluid inclusions focused on seven samples from Stages 3 and 4 (Table 1), and all analyses were performed on fluid inclusions hosted by quartz, calcite and sphalerite using a heating–freezing stage (Linkam THMSG-600) at the State Key Laboratory of Ore Deposit Geochemistry, Chinese Academy of Sciences, Guiyang, China. The temperature range of the instrument is −196 to +600 °C, and the precision and accuracy of the microthermometry measurements, based on standard calibration procedures, was estimated to be ±2 °C for homogenization temperatures and ±0.1 °C for last ice-melting temperatures. Salinity estimates were determined from the last melting temperature of ice for the NaCl–H_2O system (Bodnar, 1993). Given that calcite and sphalerite are relatively soft minerals, freezing of inclusions can lead to expansion and stretching, enlarging the vapour bubble. To avoid false homogenization temperatures, the homogenization temperature measurements were performed before the ice-melting temperature measurements. For homogenization, the temperature was initially increased at a rate of 20 °C min^{-1} until the vapour bubble began to disappear. Thereafter, the heating rate was reduced to 0.5 °C min^{-1} until the bubble completely disappeared. When the homogenization temperature measurements were completed, the temperature was decreased to −160 °C at a rate of 20 °C min^{-1} to assure completely frozen inclusions and was then slowly increased at a rate of 10 °C min^{-1}. Once the ice began to melt, the rate of heating was decreased to 0.1 °C min^{-1}. The temperature at which the last ice melted indicated the freezing-point depression of the fluid inclusions.

3.c. Laser Raman spectroscopy analysis

The compositions of selected individual fluid inclusions were determined at the State Key Lab for Mineral Deposit Research, Nanjing University, China, using a Raman microprobe (Renishaw RM2000) with an Ar ion laser. A surface power of 5 mW was used with a laser wavelength of 514.5 nm, the detector charge-coupled device (CCD) area was 20 μm^2, and the scanning range of the spectra was set to between 200 and 4000 cm^{-1}, with an accumulation time of 30 s for each scan.

3.d. Stable isotope analysis

The hydrogen isotopic compositions of the fluid inclusions and the oxygen isotopic composition of the host quartz were determined for Stages 3 and 4 (Table 4, further below). Sulphur isotope analysis focused on chalcopyrite, sphalerite, galena from sulphide ores, and gypsum of country rock (Table 5, further below). To prepare monomineralic samples, coarse purified quartz, sulphide and sulphate minerals were first separated by handpicking under a binocular microscope and then crushed and sieved. Finally, they were treated in dehydrated ethanol to remove any impurities.

For the oxygen isotope analysis, 1 g of a 200-mesh quartz sample was used, and oxygen extracted using the BrF_5 method described by Clayton & Mayeda (1963). The resultant oxygen was reacted with graphite rods to produce carbon dioxide. The oxygen isotopic compositions were determined at the State Key Laboratory of Isotopic Geology of the Ministry of Land and Resources, Beijing, China, using a stable isotope mass spectrometer (MAT-253EM). The results are given relative to V-SMOW (Vienna Standard Mean Ocean Water) (Craig, 1961; Baertschi, 1976), with a precision of ±0.2 ‰.

For the hydrogen isotope analysis, 2–3 g of a 40- to 80-mesh quartz sample was prepared. The samples were heated in an induction furnace to decrepitate fluid inclusions and release the water. The water was reduced with Zn metal in a sealed tube at 450 °C (Coleman *et al.* 1982). The hydrogen isotopic compositions were also analysed with a stable isotope mass spectrometer (MAT-253EM) at the State Key Laboratory of Isotopic Geology of the Ministry of Land and Resources. The δD values are also reported relative to V-SMOW, with an analytical precision of ±2 ‰.

For the sulphur isotope analysis, 0.05 g of a 200-mesh sulphide and gypsum samples were prepared. Each sample was reacted with Cu_2O powder to

https://doi.org/10.1017/S001675681700111X Published online by Cambridge University Press

https://doi.org/10.1017/S001675681700111X Published online by Cambridge University Press

Table 1. Representative LA-ICP-MS analyses of rhodonites.

Sample no.	LZY1071-1	LZY1071-2	LZY1062-2	LZY1062-3	LZY1062-4	LZY1062-5	LZY1056-1	LZY1056-2	LZY1056-3	LZY1033-1	LZY1033-2
Na_2O	0.01	0.01	0.01	0.01	0.00	0.00	0.02	0.02	0.02	0.02	0.01
MgO	0.65	0.67	0.62	0.65	0.53	0.43	0.62	0.66	0.61	1.29	0.59
Al_2O_3	0.01	0.01	0.01	0.03	0.00	0.02	0.00	0.00	0.01	0.06	0.01
SiO_2	47.00	47.16	47.05	47.03	47.32	47.00	47.33	47.93	47.47	38.37	39.07
P_2O_5	0.01	0.00	0.00	0.00	0.02	0.01	0.00	0.00	0.00	0.00	0.00
K_2O	0.00	0.00	0.00	0.00	0.00	0.00	0.00	0.00	0.01	0.02	0.00
CaO	8.36	8.61	9.95	8.93	8.93	8.99	9.04	8.61	8.91	14.89	14.17
TiO_2	0.00	0.00	0.00	0.00	0.00	0.00	0.00	0.00	0.00	0.00	0.00
MnO	37.02	36.70	39.22	40.00	39.69	40.54	37.95	37.95	38.11	43.29	44.50
FeO	6.72	6.60	3.01	3.22	3.33	2.85	4.82	4.62	4.67	1.61	1.44
Total	99.79	99.78	99.87	99.86	99.83	99.85	99.78	99.80	99.80	99.55	99.79
Na	0.001	0.001	0.001	0.001	0.000	0.000	0.001	0.001	0.001	0.002	0.001
Mg	0.042	0.043	0.039	0.041	0.034	0.027	0.039	0.042	0.039	0.087	0.040
Al	0.001	0.001	0.000	0.001	0.000	0.001	0.000	0.000	0.000	0.003	0.000
Si	2.002	2.005	1.997	1.999	2.008	2.000	2.008	2.025	2.012	1.735	1.762
P	0.000	0.000	0.000	0.000	0.001	0.000	0.000	0.000	0.000	0.000	0.000
K	0.000	0.000	0.000	0.000	0.000	0.000	0.000	0.000	0.000	0.001	0.000
Ca	0.382	0.392	0.453	0.407	0.406	0.410	0.411	0.390	0.405	0.722	0.684
Ti	0.000	0.000	0.000	0.000	0.000	0.000	0.000	0.000	0.000	0.000	0.000
Mn	1.333	1.319	1.407	1.437	1.424	1.458	1.361	1.355	1.365	1.654	1.696
Fe^{2+}	0.239	0.234	0.106	0.114	0.118	0.101	0.170	0.163	0.165	0.061	0.054
Total	3.998	3.995	4.003	4.000	3.991	3.999	3.992	3.976	3.988	4.265	4.238
$CaSiO_3$	19.2 %	19.8 %	22.6 %	20.4 %	20.6 %	20.5 %	20.8 %	20.3 %	20.6 %	28.2 %	27.1 %
$MnSiO_3$	66.7 %	66.1 %	70.3 %	71.9 %	71.5 %	72.9 %	68.3 %	68.5 %	68.6 %	74.8 %	77.7 %
$(Fe, Mg)SiO_3$	14.2 %	14.2 %	7.1 %	7.8 %	8.1 %	6.5 %	11.0 %	11.8 %	11.0 %	8.4 %	9.5 %

All Fe as FeO; cation proportions on the basis of 12 oxygens.

Table 2. Representative LA-ICP-MS analyses of bustamites and actinolites.

Mineral	Bustamite				Actinolite				
Sample no.	LZY1075-1	LZY1062-2	LZY1062-2	LZY1056-3	LZY0872-1	LZY0872-2	LZY0872-3	LZY0872-4	LZY0827-2
Na_2O	0.05	0.04	0.00	0.03	0.15	0.19	0.11	0.18	0.26
MgO	1.92	2.39	0.74	1.68	9.46	9.17	9.20	9.15	11.83
Al_2O_3	0.04	0.02	0.00	0.03	0.42	0.51	0.18	0.58	0.54
SiO_2	46.42	47.88	44.89	44.88	52.54	52.32	53.04	52.41	53.17
P_2O_5	0.01	0.01	0.00	0.00	0.00	0.01	0.01	0.00	0.00
K_2O	0.01	0.00	0.00	0.00	0.03	0.04	0.02	0.03	0.05
CaO	13.45	13.51	13.15	15.45	12.12	12.11	12.17	12.24	12.38
TiO_2	0.00	0.00	0.00	0.00	0.00	0.01	0.00	0.01	0.00
MnO	33.17	31.34	37.13	31.37	5.46	5.71	5.48	5.54	5.27
FeO	4.76	4.63	3.94	6.31	19.70	19.80	19.67	19.73	16.34
Total	99.83	99.82	99.84	99.76	99.87	99.87	99.88	99.87	99.84
Na	0.004	0.004	0.000	0.003	0.011	0.014	0.008	0.013	0.019
Mg	0.121	0.149	0.048	0.108	0.552	0.536	0.536	0.535	0.680
Al	0.002	0.001	0.000	0.001	0.019	0.023	0.008	0.027	0.024
Si	1.957	1.992	1.929	1.914	2.045	2.041	2.061	2.042	2.036
P	0.000	0.000	0.000	0.000	0.000	0.000	0.000	0.000	0.000
K	0.001	0.000	0.000	0.000	0.001	0.002	0.001	0.002	0.003
Ca	0.608	0.602	0.605	0.706	0.505	0.506	0.507	0.511	0.508
Ti	0.000	0.000	0.000	0.000	0.000	0.000	0.000	0.000	0.000
Mn	1.182	1.102	1.348	1.131	0.180	0.188	0.180	0.182	0.171
Fe^{2+}	0.167	0.160	0.141	0.224	0.639	0.643	0.637	0.640	0.521
Total	4.043	4.009	4.071	4.087	3.952	3.955	3.939	3.952	3.962
$CaSiO_3$	29.2 %	29.9 %	28.1 %	32.8 %	26.9 %	27.0 %	27.4 %	27.3 %	27.0 %
$MnSiO_3$	57.9 %	54.9 %	65.3 %	54.0 %	10.7 %	11.1 %	11.0 %	10.8 %	10.1 %
(Fe, Mg)SiO_3	12.0 %	15.0 %	5.2 %	11.5 %	62.9 %	62.3 %	62.7 %	62.2 %	63.2 %

All Fe as FeO; cation proportions on the basis of 12 oxygens.

produce SO_2 following the technique of Robinson & Kusakabe (1975). The SO_2 gas was gathered and purified to analyse the sulphur isotope compositions using a mass spectrometer (MAT252) at the State Key Laboratory of Ore Deposit Geochemistry, Chinese Academy of Sciences. The analytical results are reported relative to CDT (Canyon Diablo Troilite), with a precision of ±0.2 ‰.

4. Results

4.a. Rhodonite textural investigation

The textural relationship between rhodonite and other minerals was investigated in detail in this study. Exsolution textures between rhodonite and bustamite were photographed (Fig. 5d), and overprinting of sulphide and hydrous skarn minerals is also evident (Fig. 5e–h).

The evidence from both hand specimens and thin sections indicates that Stage 1 skarn minerals (rhodonite) coexisted with fibrous skarn minerals (bustamite), suggesting an exsolved textural relationship between rhodonite and bustamite. Rhodonite has $MnSiO_3$ contents of 66.1–77.7 mole %, $CaSiO_3$ contents of 19.2–28.2 mole % and (Fe, Mg)SiO_3 contents of 7.1–14.2 mole % (Table 1). Bustamite has $MnSiO_3$ contents of 54.0–65.3 mole %, $CaSiO_3$ contents of 28.1–32.8 mole %, and (Fe, Mg)SiO_3 contents of 5.2–15.0 mole % (Table 2). In hand specimen (Fig. 5a), rhodonite has a prismatic crystal shape, is pink in colour, and occurs as relict within the actinolite zone. In thin sections (Fig. 5b–d), calcite, quartz and sphalerite replace rhodonite along cleavage planes.

Sample LZY_{12}-3 shows fibrous and radiating aggregates (10 cm wide) within the marble (Fig. 5e), and sphalerite, galena and chalcopyrite occur commonly as interstitial grains or scattered crystals between the fibrous minerals (Fig. 5f–h). These fibrous minerals were determined to be actinolite with concentrations of 10.1–11.1 mole % $MnSiO_3$, 26.9–27.4 mole % $CaSiO_3$, and 62.2–63.2 mole % (Fe, Mg)SiO_3 (Table 2).

4.b. Fluid inclusion studies

4.b.1. Fluid inclusion petrography

Owing to the lack of fluid inclusions in Stages 1 and 2, only fluid inclusions from Stages 3 and 4 were investigated in this study. Based on the number of constituent phases observed at room temperature (Roedder, 1984: 12–26), combined with microthermometric behaviour, two main types of fluid inclusions were recognized:

Type 1 refers to two-phase (vapour + liquid) aqueous inclusions. They are elliptical or circular in shape, and sizes vary between 8 and 25 μm in the longest dimension (Fig. 6c–j). The vapour phase was estimated to occupy 10–50 vol. % of the inclusion. Total homogenization of all Type 1 inclusions was to the liquid phase. The Type 1 fluid inclusions occur in Stages 3 and 4.

Type 2 represents elliptical to well-rounded, non-aqueous inclusions. They show one phase of vapour

https://doi.org/10.1017/S001675681700111X Published online by Cambridge University Press

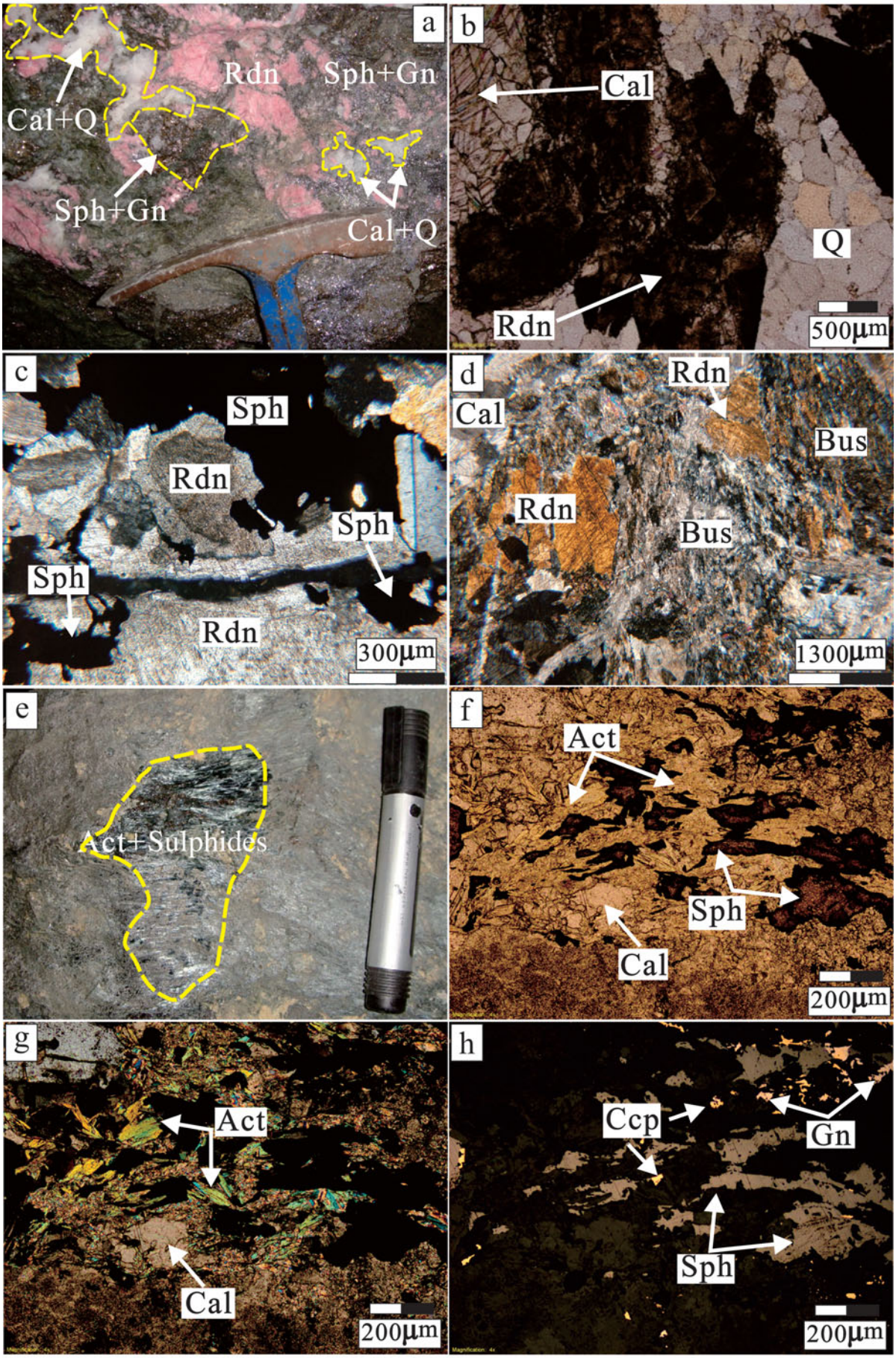

Figure 5. (Colour online) Macroscopic and microscopic features of skarn mineralization from the Luziyuan deposit. (a) Pink rhodonite overprinted by a quartz–calcite–sphalerite–galena assemblage. (b) Replacement of rhodonite by quartz and calcite along the

https://doi.org/10.1017/S001675681700111X Published online by Cambridge University Press

at room temperature, ranging in size from 8 to 10 μm in the longest dimension (Fig. 6a, b). Notably, the Type 2 fluid inclusions are of rare occurrence and occur only in Stage 3.

Fluid inclusion assemblage (FIA) refers to discriminating a group of petrographically associated fluid inclusions (Goldstein & Reynolds, 1994: 77–9). A FIA implies that the inclusions are cogenetic, forming at the same time and from the same fluid. Fluid inclusions that occur within healed microfractures or within growth zones of host mineral are easily identified as FIA. However, not all fluid inclusions could be assigned to a FIA during this study. Only the secondary inclusions occurring along healed fractures are assigned the term FIA. Here we use the abbreviation 'non-FIA' to represent the fluid inclusions which occur as isolated, irregular clusters, randomly distributed and scattered (Chi & Lu, 2008).

In Stage 3, Type 1 inclusions hosted in quartz usually show a primary origin and occur as irregular clusters (Fig. 6c), scattered (Fig. 6d) and isolated (Fig. 6e, f) with similar vapour-to-liquid (V/L) ratios (30–50 %), which represents non-FIAs (Fig. 6c–f). In Figure 6f, some Type 1 inclusions with relatively low V/L ratios (10–20 %) occur as scattered separated from isolated inclusions with V/L ratios (30–50 %) in the same grains.

In Stage 4, Type 1 inclusions hosted in calcite and sphalerite occur as non-FIAs and FIAs. The non-FIA inclusions usually occur as randomly distributed (Fig. 6h, i) and have consistent V/L ratios (V/L = 20–40 %). In contrast, the FIA inclusions occur in transgranular planar arrays or healed microcracks of quartz, calcite and sphalerite crystals (Fig. 6g, h, j). These secondary FIA inclusions have low V/L ratios (10–20 %), which represent fluid entrapment after mineral crystallization.

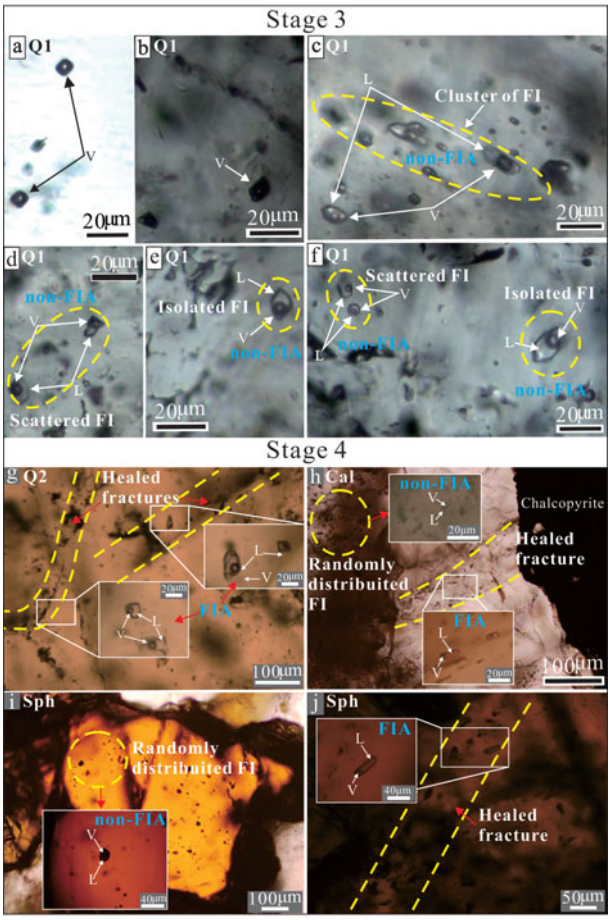

Figure 6. (Colour online) Photomicrographs of non-FIAs and FIAs hosted by quartz, calcite and sphalerite from Stages 3 and 4. (a, b) Type 2 non-aqueous fluid inclusions occur as negative shapes trapped in Stage 3 quartz. (c–f) Fluid inclusions (Type 1) within non-FIA hosted by Stage 3 quartz occur as clusters (scattered, isolated). (g) Fluid inclusions (Type 1) in Stage 4 quartz occur as FIAs along the subparallel transgranular planar arrays. (h) Fluid inclusions (Type 1) in Stage 4 calcite occur as non-FIA in random distribution, and fluid inclusions (Type 1) occur as FIA along the healed fractures. (i) Fluid inclusions (Type 1) occur as non-FIA randomly distributed in the Stage 4 sphalerite. (j) Fluid inclusions (Type 1) occur as FIA along the subparallel transgranular planar arrays in the Stage 4 sphalerite. Non-FIA – non-fluid inclusion assemblage; FIA – fluid inclusion assemblage.

4.b.2. *Microthermometry*

The microthermometric results are evaluated by FIA in these host minerals (quartz, calcite and sphalerite). The microthermometric data for the fluid inclusions in this study are summarized in Table 3 and Figures 7 and 8.

In Stage 3, non-FIA (irregular clusters) inclusions record homogenization temperatures of 320–356 °C and salinities of 16.7–21.0 wt % NaCl equivalent (Table 3; Fig. 7a, b). Additionally, three non-FIA (isolated) inclusions have higher homogenization temperatures of 354–376 °C and similar salinities of 16.2–20.4 wt % NaCl equivalent (Table 3; Fig. 7a, b). In contrast, fluid inclusions from non-FIA (scattered) reveal low homogenization temperatures between 259 and 290 °C and low salinities varying between 5.0 and 13.0 wt % NaCl equivalent (Table 3; Fig. 7a, b).

In Stage 4, homogenization temperatures and salinities for non-FIA in calcite range from 224 to 273 °C

cleavage plane under plane-polarized light. (c) Columnar rhodonite crystal (first-order grey to orange interference colour) replaced by sphalerite under crossed nicols. (d) Numerous fibrous bustamite coexists with prismatic rhodonite (orange interference colour) under crossed nicols. (e) Typical sulphide mineralization shown by small grains infilling fibrous actinolite aggregate. (f) Sulphide infilling between actinolite under plane-polarized light showing that the formation of sulphides was later than actinolite formation. (g) Actinolite showing secondary interference colours blue and green under crossed nicols. (h) Sphalerite, galena and chalcopyrite infilling between actinolite under reflected light (Rdn – rhodonite, Bus – bustamite, Act – actinolite, Q – quartz, Cal – calcite, Ccp – chalcopyrite, Sph – sphalerite, Gn – galena).

https://doi.org/10.1017/S001675681700111X Published online by Cambridge University Press

Table 3. Summary of homogenization temperatures, salinities and pressures for the studied fluid inclusions.

Ore stage	Host mineral	Mode of occurrence	FI type	T_h Range; Mean (*n*)	T_m(ice) Range; Mean (*n*)	Salinity Range; Mean (*n*)	*P* (bar) Range
Stage 3	Quartz	IC	Lv	320–356 (12)	−18.1 to −12.8 (12)	16.7–21.0 (12)	96–152
		I	Lv	354–376 (3)	−17.2 to −12.3 (3)	16.2–20.4 (3)	148–195
		S	Lv	259–290 (14)	−9.2 to −3.0 (14)	5.0–13.0 (14)	42–69
Stage 4	Calcite	RD	Lv	224–273 (8)	−8.2 to −5.4 (8)	8.4–11.9 (8)	23–53
		HF	Lv	167–207 (14); 193	−6.5 to −1.3 (14); −4.0	2.2–9.9 (14); 6.4	7–17
	Sphalerite	RD	Lv	232–246 (5)	−18.6 to −8.8 (5)	12.6–21.4 (5)	25–33
		HF	Lv	168–207 (4); 188	−6.5 to −3.0 (4); −5.2	4.9–9.8 (4); 8.0	7–17
	Quartz	HF	Lv	161–209 (12); 194	−2.9 to −1.3 (12); −2.1	2.2–4.8 (12); 3.6	6–18

IC = irregular cluster; I = isolated; S = scattered; RD = randomly distributed; HF = healed fracture; numbers in brackets represent inclusion numbers. HF is fluid inclusion assemblage (FIA), and the others are non-FIAs. FI = fluid inclusion; Lv = liquid-vapour fluid inclusions; T_h = homogenization temperature; T_m(ice) = temperature of final ice melting; P = minimum pressure; temperatures in °C; salinities in wt % NaCl equiv.

Table 4. Hydrogen isotopic composition of fluid inclusions hosted by quartz and oxygen isotope composition of quartz from the Luziyuan Pb–Zn skarn deposit.

Sample number	Studied lithology	Mineral	Mineralization stage	$^{18}O_{V\text{-}SMOW}$‰	T (°C)	$\delta^{18}O_{H2O}$‰	$\delta D_{V\text{-}SMOW}$‰
LZY_{10}-19	Stage 3 coarse barren quartz vein	Q_1	Stage 3	12.8	333	6.7	−72
LZY_{10}-11	Stage 3 coarse barren quartz vein	Q_1	Stage 3	15.7	333	9.6	−78
LZY_{12}-68	Stage 3 coarse barren quartz vein	Q_1	Stage 3	12.6	333	6.5	−81
LZY_{12}-38	Stage 3 coarse barren quartz vein	Q_1	Stage 3	12.5	333	6.4	−118
LZY_{12}-39	Stage 3 coarse barren quartz vein	Q_1	Stage 3	11.4	333	5.3	−103
LZY_{12}-32	Stage 4 quartz-sphalerite vein	Q_2	Stage 4	12.9	247	3.7	−98
LZY_{12}-67	Stage 4 quartz-sphalerite ± galena-calcite vein	Q_2	Stage 4	12.6	247	3.4	−100
LZY_{10}-50	Stage 4 quartz-galena vein	Q_2	Stage 4	12.3	247	3.1	−103
LZY_{12}-75-9	Stage 4 quartz-sphalerite vein	Q_2	Stage 4	12.4	247	3.2	−85
LZY_{12}-62	Stage 4 quartz-sphalerite ± galena-calcite vein	Q_2	Stage 4	11.9	247	2.7	−109

Q_1 = quartz hosted by Stage 3; Q_2 = quartz hosted by Stage 4. $\delta^{18}O_{H2O}$‰ values were calculated based on the quartz–H_2O oxygen isotope fractionation equation of Zheng (1993), and temperatures (*T*) are based on micothermometric data from non-FIA inclusions in Stages 3 and 4.

and from 8.4 to 11.9 wt % NaCl equivalent, respectively (Table 3; Fig. 7c, d), which are similar values to those of non-FIA (scattered) in Stage 3, whereas fluid inclusions from FIA in calcite exhibit low homogenization temperatures (167–207 °C) and salinities (2.2–9.9 wt % NaCl equivalent). Non-FIAs in sphalerite have similar homogenization temperatures (232–246 °C) to inclusions in calcite, but higher salinities (12.6–21.4 wt % NaCl equivalent) (Table 3; Fig. 7e, f). FIA in sphalerite shows similar homogenization temperatures (168–207 °C) and salinities (4.9–9.8 wt % NaCl equivalent) to FIA in calcite (Table 3; Fig. 7e, f). FIA in quartz shows analogous homogenization temperatures (161–209 °C) and salinities (2.2–4.8 wt % NaCl equivalent) (Table 3; Fig. 7g, h) to calcite and sphalerite.

In the homogenization temperature v. salinity diagram (Fig. 8), the fluid inclusion data from the three minerals from Stages 3 and 4 show the following characteristics: for non-FIA inclusions in Stage 3 quartz, it seems that non-FIA (irregular cluster) fluid inclusion data for 1495 are the same as non-FIA (isolated) inclusion data for 1265, non-FIA (scattered) inclusion data are nearly the same for all three levels and have lower homogenization temperature and salinity compared to non-FIA (irregular cluster and isolated); non-FIA inclusions from the calcite and sphalerite in Stage 4 again show the same homogenization temperatures for 1220 and 1265 respectively; the secondary FIA inclusions in calcite, sphalerite and quartz are always lower in homogenization temperature and salinity compared to non-FIA inclusions for all levels.

4.b.3. Laser Raman spectroscopy

The gas compositions of representative fluid inclusions in quartz crystals from Stages 3 and 4 were determined by laser Raman spectroscopy. The analyses of Stage 3 non-aqueous fluid inclusions show that CH_4 is the dominant component (Fig. 9a). The vapour phase composition of the Stage 4 aqueous two-phase (vapour–liquid) inclusions is mainly composed of H_2O, with no other compressive volatile components (Fig. 9b).

4.c. Stable isotope studies

4.c.1. Hydrogen and oxygen isotopes

The hydrogen isotopic composition of the fluid inclusions in quartz and the oxygen isotopic composition of the quartz grains from Stages 3 and 4 were investigated. The results of the analyses are summarized in Table 4. The oxygen isotopic composition of the fluid in equilibrium with the quartz was calculated

https://doi.org/10.1017/S001675681700111X Published online by Cambridge University Press

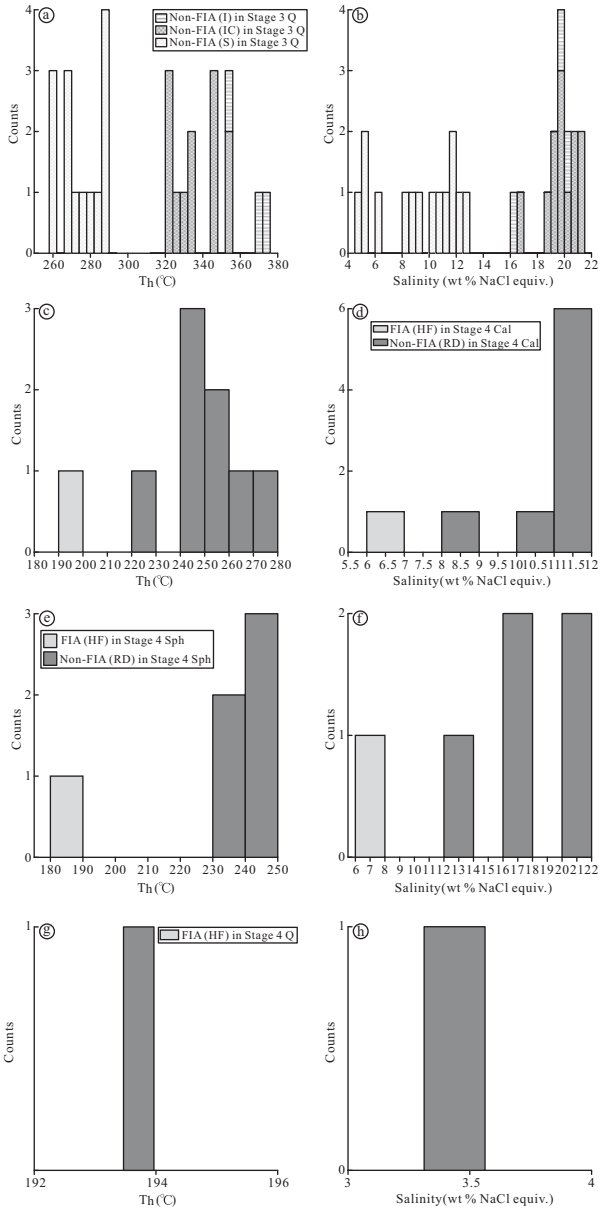

Figure 7. Histograms showing homogenization temperatures (Th) and salinity for non-FIA and FIA inclusions in the Luziyuan deposit. (a, b) Th and salinity histograms of non-FIA (I, C and S) inclusions in Stage 3 quartz; (c) d-Th and salinity histograms of non-FIA (RD) and FIA (HF) inclusions in Stage 4 calcite; (e) f-Th and salinity histograms of non-FIA (RD) and FIA (HF) inclusions in Stage 4 sphalerite; (g) h-Th and salinity histograms of FIA inclusions in Stage 4 quartz. I – isolated; IC – irregular cluster; S – scattered; RD – randomly distributed; HF – healed fracture; Q – quartz; Cal – calcite; Sph – sphalerite.

using appropriate fractionation factors (see footnote to Table 4).

The calculated oxygen and hydrogen isotopic compositions of the fluid inclusions from Stage 3 quartz have similar $\delta^{18}O_{fluid}$ values but much lower δD values ($\delta^{18}O_{fluid}$ = 5.3–9.6 ‰, δD = −118 to −72 ‰) than magmatic water dissolved in felsic melts ($\delta^{18}O$ = 5.5–10.0 ‰, δD = −50 to −85 ‰; Taylor, 1997). In contrast, the calculated oxygen and hydrogen isotopic compositions of the Stage 4 fluid yield much lower $\delta^{18}O_{fluid}$ and δD values ($\delta^{18}O_{fluid}$ = 2.7–3.7 ‰, δD = −109 to −85 ‰). The hydrogen isotopic compositions of the fluid inclusions in Stage 3 quartz (δD = −90.4 ± 19.4 ‰, n = 5) and Stage 4 quartz (δD = −99.0 ± 8.9 ‰, n = 5) are similar and have a wide range of values.

Table 5. Sulphur isotope data of sulphides from the Luziyuan Pb–Zn skarn deposit.

	$\delta^{34}S$ (‰,V-CDT)			
Sample number	Sphalerite	Galena	Chalcopyrite	Gypsum
LZY_{12}-5	11.1			
LZY_{12}-7	11.1			
LZY_{12}-8	11.1			
LZY_{12}-9	11.2			
LZY_{12}-10			13.3	
LZY_{12}-11			12.4	
LZY_{12}-12	12.5			
LZY_{12}-12			12.5	
LZY_{12}-16		11.2		
LZY_{12}-19		12.7		
LZY_{12}-20		12.6		
LZY_{12}-32	12.1			
LZY_{12}-33-5	14.0			
LZY_{12}-33-5		10.9		
LZY_{12}-33-7	12.6			
LZY_{12}-33-10	12.2			
LZY_{12}-36	12.8			
LZY_{12}-39	12.3			
LZY_{12}-44	12.2			
LZY_{12}-50			12.4	
LZY_{12}-58	11.9		11.8	
LZY_{12}-59	11.8		11.6	
LZY_{12}-60	9.9			
LZY_{12}-71			14.2	
LZY_{12}-74	11.5	10.9		
LZY_{12}-74-1	11.2			
LZY_{12}-74-3		10.6	11.5	
LZY_{12}-74-10			13.9	
LZY_{12}-75-3	10.6	10.9		
LZY_{12}-75-10	12.7		12.2	
FBB_{12}-1				17.0
FBB_{12}-2				17.1
FBB_{12}-3				16.9
Mean	11.8	11.4	12.6	17.0
Min	9.9	10.6	11.5	16.9
Max	14.0	12.7	14.2	17.1
n	19	7	10	3

4.c.2. *Sulphur isotopes*

Sulphur isotope ratios for sulphides associated with the hydrothermal mineralization of the Luziyuan deposit are presented in Table 5. The $\delta^{34}S$ values for the sulphides range from 9.9 to 14.2 ‰ and have a mean of 11.9 ‰ (n = 35). The $\delta^{34}S$ values of these sulphides are much higher than the $\delta^{34}S$ values published for major Pb–Zn skarn deposits in the BND belt, such as the Jinchang (Chen, Huang & Lu, 2009) and Hetaoping deposits (Gao *et al.* 2011), and in other parts of the world, such as the Bajiazi (Zhao *et al.* 2003) and Trepca deposits (Palinkas *et al.* 2013) (Table 5). Furthermore, the $\delta^{34}S$ values of these sulphides have a prominent homogeneity and show a tower-like frequency distribution (Fig. 10). These results indicate that the $\delta^{34}S$ values of sulphides are nearly consistent (chalcopyrite: 12.6 ± 0.94 ‰, sphalerite: 11.8 ± 0.87 ‰ and

https://doi.org/10.1017/S001675681700111X Published online by Cambridge University Press

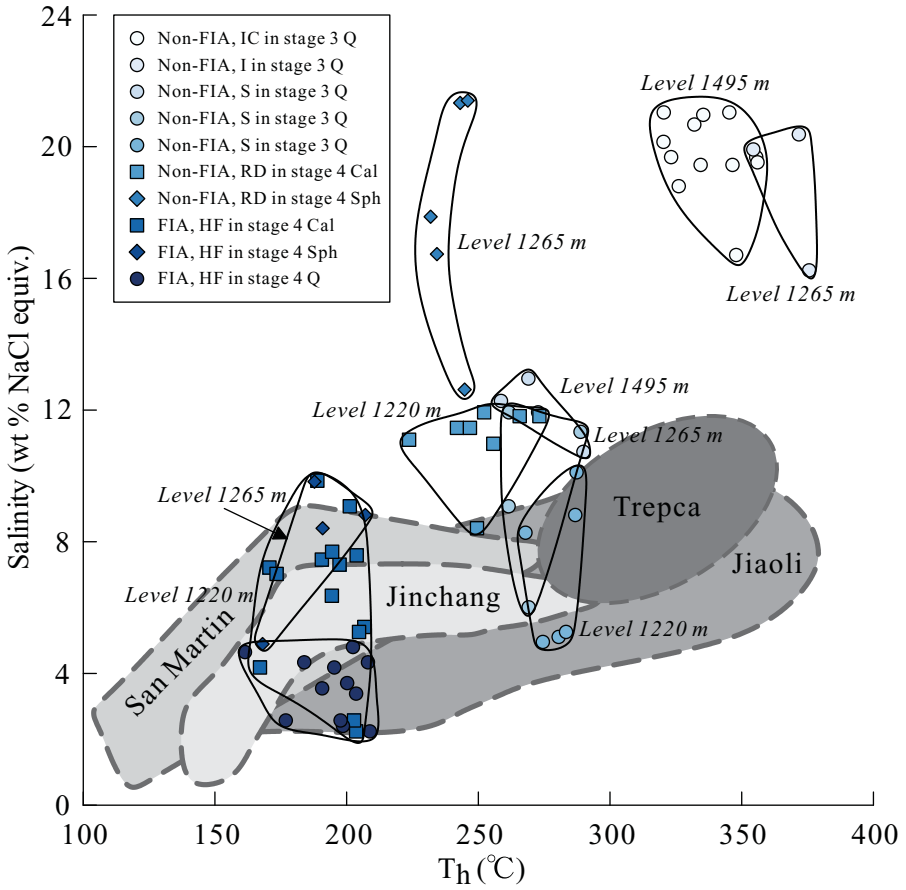

Figure 8. (Colour online) Homogenization temperature vs salinity for non-FIAs and FIAs in Stages 3 and 4 from different levels of the Luziyuan deposit together with data from other distal Pb–Zn skarn deposits, such as the Jinchang (Chen, Huang & Lu, 2009), Jiaoli (Li & Zhao, 2004), San Martin (González-Partida & Camprubí, 2006). Abbreviations are the same as those in Figure 7.

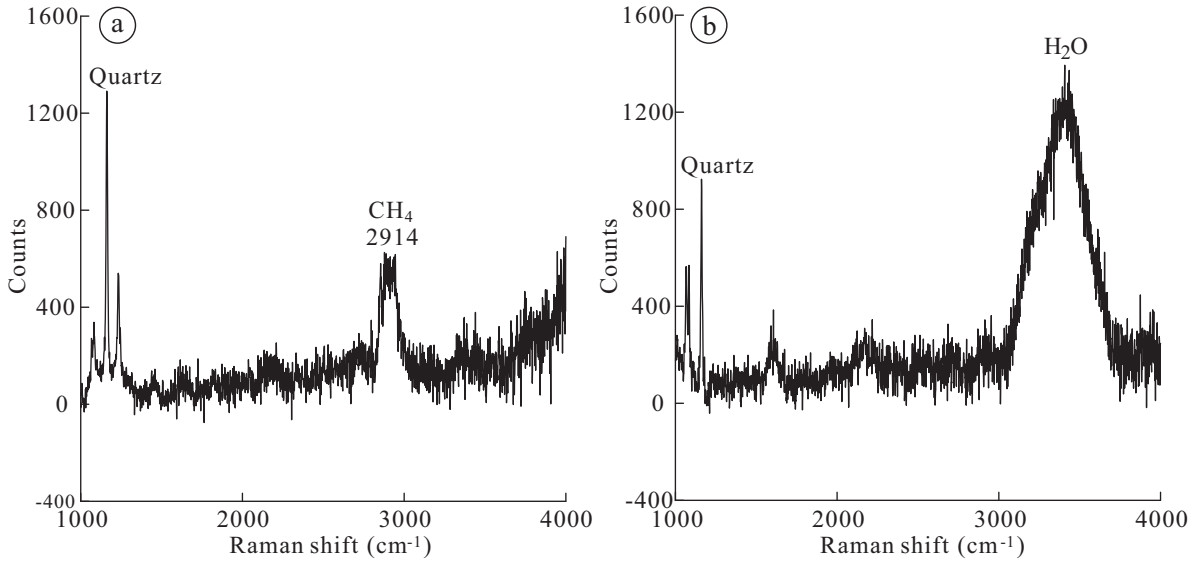

Figure 9. Representative Raman spectra of fluid inclusions in quartz from Stages 3 and 4. (a) CH_4 spectra of vapour in non-aqueous inclusions in quartz from Stage 3; (b) H_2O spectrum of vapour in biphase (vapour + liquid) aqueous inclusions from Stage 4.

https://doi.org/10.1017/S001675681700111X Published online by Cambridge University Press

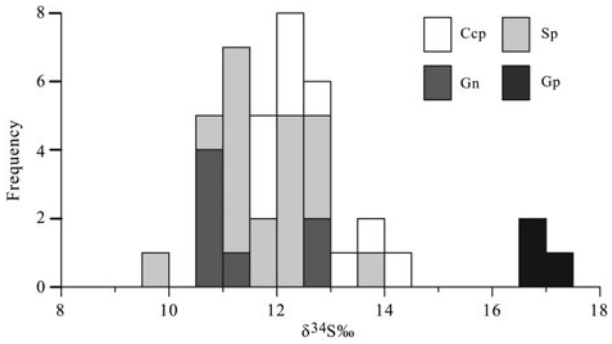

Figure 10. Frequency histogram of sulphur isotopes for chalcopyrite (Ccp), sphalerite (Sp), galena (Gn) and gypsum (Gp).

galena: 11.4 ± 0.93 ‰) and markedly lower than that of gypsum (16.9–17.1 ‰) samples from the host rock.

5. Discussion

5.a. Textural relationship between rhodonite and other minerals

The genesis and formation conditions of rhodonite have previously been investigated on the basis of petrography, theoretical considerations and experimental data (Abrecht & Peters, 1980; Brown, Essene & Peacor, 1980; Winter, Essene & Peacor, 1981; Abrecht, 1985, 1989; Cabella, Gaggero & Lucchetti, 1991; Mohapatraa & Nayak, 2005). Those authors suggested that the complex genesis of rhodonite corresponds to different formation conditions (e.g. temperature, pressure, CO_2 fugacity, O_2 fugacity, water activity, and Mn^{2+}/Ca^{2+} ratio in the fluid). Winter, Essene & Peacor (1981) reported that the rhodonite–pyroxmangite transformation in the system $MnSiO_3$ occurs at 575 °C for pressures of +8 to –9 kbar. Mohapatraa & Nayak (2005) studied the genesis of rhodonite from the metamorphosed Mn carbonate–silicate rocks, and considered that rhodonite was produced through the mineral reaction (Kutnahorite + Quartz → Rhodonite + CO_2) and this mineral reaction is influenced by the protolithic bulk composition, variation in XCO_2 (<0.2 to ~0.3) and different oxygen fugacities rather than the metamorphic temperature. Cabella, Gaggero & Lucchetti (1991) discussed the formation conditions of Mn–silicate and carbonate assemblages on the basis of the system SiO_2–MnO–CaO–CO_2–O_2, and considered that braunite-rhodonite-, johannsenite- and calcite-bearing assemblages equilibrated through mineral reactions (e.g. braunite + quartz → rhodonite + O_2) at constant P–T conditions ($P = 2.5 \pm 0.5$ kbar; $T = 275 \pm 25$ °C) as a result of progressive infiltration of Ca-rich, CO_2-bearing, relatively reducing hydrous fluids. Abrecht (1989) reported that hydrous Mn-silicates (e.g. friedelite) were formed during retrograde metamorphism by alteration of anhydrous Mn-silicates (e.g. rhodonite) through mineral reaction (e.g. tephroite + rhodonite + H_2O + HCl = friedelite). Abrecht (1985) investigated the formation conditions of two occurrences of rhodonite from the Pb–Zn–Cu skarn deposits from three mines (Empire Mine, New Mexico, USA; Monte Civillina, Italy; Valle del Temperino, Italy). One occurrence is that of submicroscopic intergrowths between prismatic rhodonite and fibrous bustamite, which was formed at the temperature below the clinopyroxene–bustamite stability field through mineral reaction ($CaMnSi_2O_6$ (cpx) + Mn(2+) = (Mn, Ca)SiO_3(rdn) + Ca(2+)) due to increasing Mn activity in the hydrothermal solution. The other occurrence is euhedral rhodonite occurring together with calcite + quartz, which was formed at equilibrium temperatures ($T = 385$ °C), pressures ($P = 1$ kbar), and CO_2 fugacity ($XCO_2 = 0.1$) through mineral reaction ($CaMnSi_2O_6$ (cpx) + CO_2 = $MnSiO_3$ (rdn) + $CaCO_3$ + SiO_2).

Based on investigation of the formation conditions of rhodonite by the authors mentioned above, rhodonite in metamorphosed Mn deposits and Pb–Zn skarn deposits is formed by either phase transformation or mineral reactions corresponding to different formation conditions. However, the exsolution of the bustamite can lead to the formation of rhodonite, and its formation conditions have been discussed by some workers (Abrecht & Peters, 1980; Brown, Essene & Peacor, 1980). Brown, Essene & Peacor (1980) discussed the subsolidus phase relations in ternary systems ($CaSiO_3$–$MgSiO_3$–$MnSiO_3$ and $CaSiO_3$–$FeSiO_3$–$MnSiO_3$) and estimated that the P–T conditions for the exsolved bustamite and rhodonite were 6 kbar at 550 °C on the basis of calcite–dolomite thermometry. However, these conditions were not confirmed by the bustamite exsolution experiment. In contrast, experimental studies of bustamite exsolution (Abrecht & Peters, 1980) indicated that the coexistence of rhodonite and bustamite forms by the bustamite exsolution at temperatures between 600 and 1100 °C and pressure of 2 kbar, and is strongly T-dependent and to a lesser extent pressure-dependent. Furthermore, Abrecht & Peters (1980) calculated that the equilibrium temperatures for natural rhodonite–bustamite assemblages of Ravinella di Sotto (Ivrea zone, Italy) and Broken Hill (New South Wales, Australia) are at 500–550 °C based on the experimental data. Therefore, the exsolved bustamite and rhodonite from Luziyuan skarn deposit suggests a temperature of at least 500 °C. In this study, as an early-stage skarn mineral, rhodonite is widespread in the Luziyuan district. As stated earlier, the petrographic evidences indicate that the prismatic rhodonite coexists with fibrous bustamite (Fig. 5d), which is replaced by the assemblage of calcite and quartz (Fig. 5b). In Figure 11, the rhodonite and bustamite compositions plot into the bustamite–rhodonite miscibility gap at $T = 550$ °C as expected by Abrecht & Peters (1980). Therefore, the observed coexistence of rhodonite and bustamite suggests that the bustamite exsolution formed as proposed by Abrecht & Peters (1980). Thus, the textural characteristics are

https://doi.org/10.1017/S001675681700111X Published online by Cambridge University Press

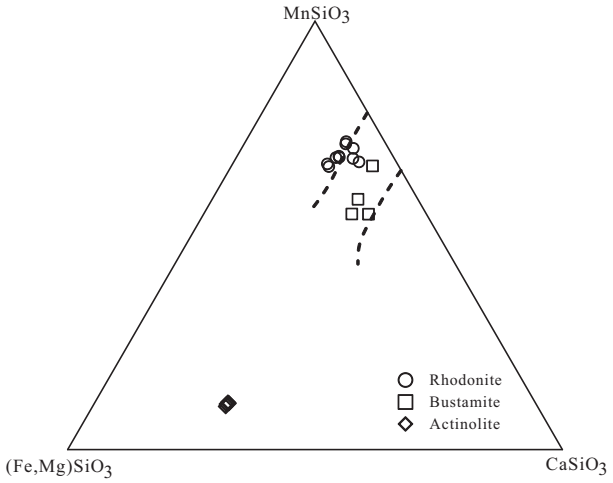

Figure 11. Mn–Ca-(Fe + Mg) plot of pyroxenoid compositions from the Luziyuan mine. Dashed lines indicate miscibility gap between rhodonite and bustamite at $T = 550\,°C$ (Abrecht & Peters, 1980).

reconciled with the exsolved bustamite and rhodonite, suggesting that the estimated temperature of the rhodonite-formation fluid was at least 500 °C.

5.b. Temperature and salinity of the Stages 3 and 4 ore fluids

As mentioned above, fluid inclusions in quartz from Stage 3 occur as non-FIAs including irregular clusters, isolated and scattered, whereas fluid inclusions in calcite and sphalerite from Stage 4 occur as non-FIAs and FIAs, and fluid inclusions in quartz from Stage 4 only occur as FIAs. The data obtained from these fluid inclusions in Stage 3 show distinct populations (Fig. 8); fluids from non-FIAs (irregular clusters and isolated) in Stage 3 have higher temperature and salinity than non-FIAs (scattered) in the same stage. Furthermore, the lower-temperature and -salinity fluids from non-FIAs (scattered) may suggest that mixing with dilute and cooler fluids, probably of meteoric origin, occurred after equilibration of early magmatic fluids. This process is suggested by the remarkable decrease of both temperature and salinity values (Fig. 8).

Apart from fluids from non-FIAs in sphalerite, fluids from non-FIAs in Stage 4 have lower temperature and salinity than in Stage 3 (Fig. 8). The overlap between the microthermometry data from non-FIAs (scattered) in Stage 3 and non-FIAs in Stage 4 (Fig. 8), also indicating non-FIAs in Stage 4, record mixing with dilute and cooler meteoric water. By contrast, fluids from FIAs in Stage 4 have the lowest observed temperature and salinity. Such characteristics may suggest that substantial mixing with dilute and cooler fluids, probably of meteoric origin, occurred during Stage 4 mineralization.

The salinities of the fluid inclusions from non-FIAs in sphalerite and calcite are markedly different (Fig. 8), such that those in calcite are typically lower than those in sphalerite (Fig. 8). Based on fluid inclusion petrographic investigations, such high-salinity inclusions in sphalerite occupy only a relatively small population (10–25 %): only five fluid inclusion data record such high salinity, whereas the majority of relatively low-salinity inclusions are recorded in calcite during Stage 4 mineralization. These features may suggest that the high-salinity inclusions in sphalerite were trapped during small portions of the sulphide stage, whereas the inclusions in calcite were trapped throughout the whole sulphide stage. Further discussion of such high-salinity fluids in sphalerite will be presented below.

Figure 8 also shows data of fluid inclusions from distal skarn-type Pb–Zn ores, such as the Jinchang (Chen, Huang & Lu, 2009), Jiaoli (Li & Zhao, 2004), San Martin (González-Partida & Camprubí, 2006) and Trepca orebodies (Palinkas *et al.* 2013). These ore deposits are controlled by structure and lithology, which are spatially related to granitic plutons.

Temperature–salinity trends in most of these deposits have been ascribed to mixing of high-temperature saline fluids of either possible or demonstrated magmatic origin, with low-temperature, low-salinity meteoric waters. Meteoric waters have been recognized as a major source of ore fluids for some deposits (Jinchang, Jiaoli, San Martin). Magmatic fluid has been recognized as an important source of ore fluids in the Trepca orebodies. Fluid mixing has been recognized, along with fluid-host interactions, as an important ore deposition mechanism in these deposits. In the Luziyuan deposit, the non-FIA (scattered) inclusions in Stage 3 and secondary FIA inclusions in Stage 4 seem to overlap with some of the fields of other skarns, indicating a significant input of meteoric waters. However, the non-FIAs (irregular cluster and isolated) in Stage 3 have higher homogenization temperature and salinity than inclusions from other skarns, representing a magmatic fluid. The non-FIA inclusions in Stage 4 show slightly lower homogenization temperature than Trepca skarn, but the former have relatively high salinity, which is discussed below.

The homogenization temperature and salinity of two-phase aqueous fluid inclusion assemblages (such as non-FIAs and FIAs) can be used to estimate the minimum pressure of fluid entrapment (Bodnar, Burnham & Sterner, 1985; Bodnar & Vityk, 1994; Driesner & Heinrich, 2007; Steele-Macinnis, Lecurnberri-Sanchez & Bodnar, 2012). Due to the absence of fluid boiling assemblages in the Luziyuan deposit, the actual trapping conditions of the fluid cannot be estimated (Roedder & Bodnar, 1980). However, the minimum pressures of fluid entrapment in Stages 3 and 4 were calculated based on the HokieFlincs_H_2O-NaCl software of Steele-Macinnis, Lecurnberri-Sanchez & Bodnar (2012). The Stage 3 fluid inclusion data measured in non-FIAs reveal the minimum formation pressure in the wide range between 96 and 195 bar (Table 3; Fig. 12), and the Stage 4 fluid inclusion data measured in non-FIAs would indicate a relatively low minimum pressure of

https://doi.org/10.1017/S001675681700111X Published online by Cambridge University Press

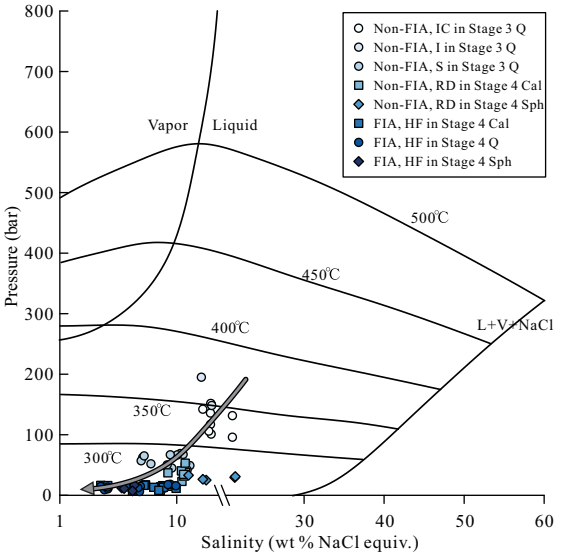

Figure 12. (Colour online) Phase diagram for the NaCl–H_2O system (Driesner & Heinrich, 2007) showing all aqueous inclusion assemblages that homogenize by vapour disappearance. Abbreviations are the same as those in Figure 7.

entrapment of 23–53 bar (Table 3; Fig. 12). Notably, the Stage 3 ore fluids have the highest pressure and show a pressure decrease associated with the depth decrease (Fig. 12); the Stage 4 ore fluids show lower pressure than Stage 3 and have nearly the same pressure for all three levels, whereas post-ore fluids from secondary FIAs show the lowest pressure and nearly the same pressure for all three levels (Fig. 12). The above evidence suggests that fluids derived from the deep concealed intrusion beneath the Luziyuan ore district may have migrated upwards to the host rocks.

5.c. Source of the ore-forming fluids

The features of early fluids of Pb–Zn skarn deposits have been revealed for the Zacatepec Pb–Zn–Ag deposit in Oaxaca (Canet *et al*. 2011) and the Trepčˇa Pb–Zn–Ag deposit in Kosovo (Palinkaš *et al*. 2013). These studies have shown that the fluids in the hydrous skarn stage and sulphide stage are dominated by meteoric waters with low temperature and salinity. However, Zhao *et al*. (2003) suggested that the fluids in the hydrous skarn stage and sulphide stage are magmatic water.

Therefore, it is unclear that the fluids in the hydrous skarn stage and sulphide stage are either meteoric waters or magmatic waters. In the case of the Luziyuan deposit, the origin of the ore-forming fluid from Stages 3 and 4 is discussed on the basis of the hydrogen isotope data from fluid inclusions hosted by quartz and by the oxygen isotope data of quartz. The $\delta^{18}O_{fluid}$ values in the Luziyuan Pb–Zn skarn deposit decrease from early to late stages. This is supported by Figure 13, which shows an isotopic shift in oxygen towards the meteoric waterline from Stage 3 to 4. Notably, both Stages 3 and 4 have extremely low δD_{fluid} values (−118 to −72 ‰ and −109 to −98 ‰, respectively). Compared with the composition of Meso-Cenozoic meteoric water in the regimes of the 'Sanjiang' middle belt ($\delta D_{fluid} = -110$ ‰ to −90 ‰; Xu & Mo, 2000), the hydrogen data from Stage 3 quartz have relatively high δD_{fluid} values, except for one sample ($\delta D_{fluid} = -118$ ‰). The extremely low δD_{fluid} values have been ascribed to either boiling (Giggenbach, 2003; Seghedi *et al.* 2007; De Hoog, Taylor & Van Bergen, 2009) or reactions within organic-matter-rich metasedimentary rocks (Sheppard, 1986; Moura, 2008). However, petrographic evidence for boiling has not been observed in this study; instead, three CH_4-rich fluid inclusions hosted in Stage 3 quartz have been identified (Fig. 9a). Hence, the low δD_{fluid} value ($\delta D_{fluid} = -118$ ‰) can be interpreted to be the result of reactions with organic-matter-rich metasedimentary rocks. The hydrogen data from Stage 4 quartz ($\delta D_{fluid} = -109$ to −98 ‰) are in good agreement with those of meteoric water ($\delta D_{fluid} = -110$ to −90 ‰). For the hydrogen and oxygen isotopic evolution of the Luziyuan deposit, this trend indicates mixing between early magmatic water with high $\delta^{18}O_{fluid}$ and δD_{fluid} values and meteoric water with relatively low $\delta^{18}O_{fluid}$ and δD_{fluid} values, with greater contributions of meteoric water to the ore fluids in Stage 4.

High-salinity fluids, such as those present during Stage 4 mineralization, are typically produced by (1) seawater evaporation, (2) dissolution of halite or other evaporites or (3) the segregation of exsolved magmatic water. The $\delta^{34}S$ compositions from the Luziyuan deposit are consistent with those of a gypsum layer from Ordovician strata exposed in the Luziyuan region (Fig. 10). The high $\delta^{34}S$ values of sulphides in this deposit may reflect thermochemical sulphate reduction because of the extremely low isotopic fractionation between sulphides and sulphates (Ohmoto, Kaiser & Geer, 1990; Hoefs, 1997: 201). Moreover, as confirmed by the Raman data, the non-aqueous fluid inclusions are rich in CH_4, which indicates that a reducing ore fluid is responsible for this deposit. Therefore, the sulphur species of the ore-forming fluid are dominated by H_2S, and the $\delta^{34}S$ values of the hydrothermal system were hardly influenced by deposition of sulphides (Ohmoto & Rye, 1979: 509–67). This may explain why the ore fluid in this deposit has high $\delta^{34}S$ values. The presence of the gypsum from host rock, with its associated isotopic signature, is distinct from other similar types of major Pb–Zn skarn deposits (Table 6), and its signature in the Luziyuan ore fluid suggests that this gypsum was the main source of sulphur for the ore-forming fluids during the formation of the Luziyuan deposit. Overall, the high-salinity fluid associated with the Stage 4 mineralization may have interacted with the gypsum layer, thus ruling out seawater evaporation and magmatic waters. Such a scenario would also explain why the fluid inclusions do not become less saline between Stages 3 and 4. Overall, both the fluid inclusion and stable isotope evidence suggests that the Luziyuan ore fluids were derived from two sources,

https://doi.org/10.1017/S001675681700111X Published online by Cambridge University Press

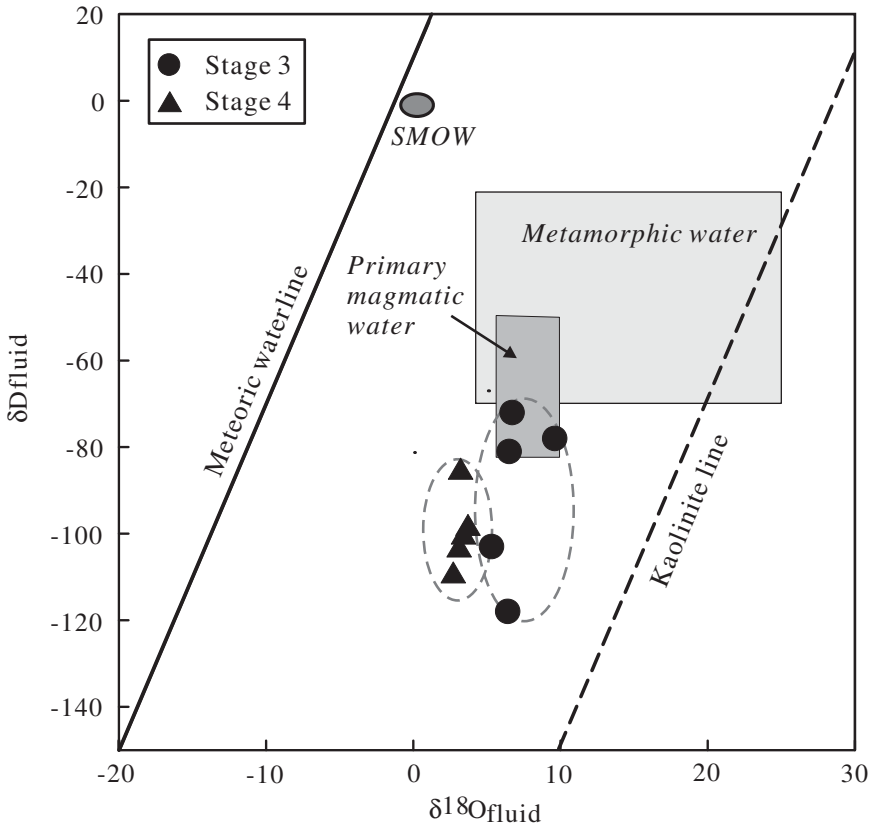

Figure 13. Plot of δD v. $\delta^{18}O$ for Stage 3 and 4 fluids (fields showing δD and $\delta^{18}O$ of metamorphic and primary magmatic water are after Taylor (1997).

Table 6. Summary of sulphur isotope data for the described Pb–Zn skarn deposit.

		$\delta^{34}S$(‰,V-CDT)			
Deposit	Mineral	Range	Mean	*n*	Data source
Jinchang	Sph/Gn	−1.9 to 5.3	1.7	18	Chen, Huang & Lu (2009)
Hetaoping	Sph/Gn/Py	3.8–7.2	6.0	11	Gao *et al*. (2011)
Bajiazi	Py	−6.9 to 3.8	0.9	9	Zhao *et al*. (2003)
Trepca	Sph/Gn/Py/Po	−5.2 to 10.0	3.3	60	Palinkas *et al*. (2013)
Luziyuan	Sph/Gn/Ccp/Gp	9.9–17.1	12.3	39	This paper

Sph = sphalerite, Gn = galena, Py = pyrite, Po = pyrrhotite, Ccp = chalcopyrite, Gp = gypsum.

magmatic fluids and meteoric water, and were simultaneously influenced by the dissolution of evaporites (an Ordovician gypsum layer) occurring in the Luziyuan region.

5.d. Ore deposit genesis

The Luziyuan deposit formed in the early Yanshanian (183 ± 2.3 Ma, Sm–Nd age of calcite; Yang, 2013) in response to collision between the Tengchong terrane and the Baoshan terrane (Mo & Pan, 2006). Yanshanian granitic plutons are not exposed in the Luziyuan region. However, a concealed intermediate-acidic intrusion in the area was indicated by geophysical exploration (Li & Mo, 2001) and is considered to be related to the Muchang intrusion (Ye *et al.* 2010). The country rocks are marble and slate of the upper Cambrian Shahechang Formation, and a large number of Mn-bearing skarn minerals (e.g. rhodonite) are present. The ore-forming fluids were derived mainly from magmatic water with some input of meteoric water during the late mineralization stage, based on fluid inclusion data and H and O isotopic data. The Luziyuan Pb–Zn deposit shares a number of common features with distal Pb–Zn skarn deposits worldwide, including the tectonic setting, concealed intermediate-acidic intrusion, skarn minerals and mineralization fluids (Einaudi, Meinert & Newberry, 1981; Meinert, 1987; Newberry, 1987; Megaw, Ruiz & Titley, 1988; Li & Zhao, 2004; Yang *et al.* 2013). These similarities support our viewpoint that it is a distal Pb–Zn skarn deposit. Additionally, the Luziyuan Pb–Zn skarn deposit has another distal characteristic: it contains elevated Co and depleted In contents, a pattern that is

https://doi.org/10.1017/S001675681700111X Published online by Cambridge University Press

significantly different from that of proximal Cu–Fe skarn deposits based on the LA-ICP-MS analysis of sphalerite (Ye *et al.* 2011*a*).

A metallogenic model for the Luziyuan deposit can be derived by combining the findings of the fluid inclusion and stable isotope results with the field and textural observations. The emplacement of a concealed intrusive body produced a relatively high-temperature, high-salinity magmatic fluid. This magmatic fluid became relatively enriched in Pb and Zn as it migrated upwards through the marble and slate of the upper Cambrian Shahechang Formation, which is known to be enriched in Pb (325 ppm) and Zn (420 ppm) (Dong & Chen, 2007). The migration of this fluid to the site of the carbonate host rock resulted in a reaction that generated the Stage 1 anhydrous phases (garnet and rhodonite) and Stage 2 hydrous skarn minerals (actinolite and chlorite). During Stages 3 and 4, the ore fluid mixed with meteoric water, which involved the dissolution of a gypsum layer in the overlying Ordovician strata, causing metals such as Pb and Zn to precipitate as sulphides.

6. Conclusions

Skarn mineral chemistry, microthermometric and Raman spectroscopic data, in combination with H–O–S isotope data, allow some important conclusions to be drawn about the origin of the ore-forming fluid and mechanisms that control the formation of the Luziyuan skarn-type Pb–Zn deposit:

(1) Four paragenetic stages are developed in the Luziyuan deposit: Stage 1, the anhydrous skarn-forming stage (garnet–rhodonite–bustamite assemblage); Stage 2, the hydrous skarn-forming stage (actinolite–chlorite assemblage); Stage 3, the early quartz stage; and Stage 4, the later sulphide-forming stage (sphalerite, galena and chalcopyrite-quartz–calcite assemblage).

(2) The exsolved bustamite and rhodonite indicate an estimated skarn-forming fluid temperature of 500 °C during Stage 1 mineralization.

(3) The high-salinity inclusions in Stage 4 sphalerite are attributed to the dissolution of evaporites (an Ordovician gypsum layer) in the Luziyuan region.

(4) Fluid inclusions and H–O isotopes indicate that fluid mixing between magmatic water and meteoric water took place during the sulphide stage, which caused metals such as Pb and Zn to precipitate as sulphides.

Acknowledgements. This research project was jointly supported by the National Natural Science Foundation of China (Grant No. 41173063); the 12th Five-year Plan Project of State Key Laboratory of Ore-deposit Geochemistry, Chinese Academy of Sciences, Guiyang, China (Grant No. SKLODG-ZY125-02); and the National '973 Project' (Grant No. 2014CB440900). We are greatly indebted to Chief Engineer Zhou Yunman (Yunnan Geology and Mineral Resources Ltd.), who assisted with sampling.

Declaration of interest

There are no known conflicts of interest associated with this publication.

References

Abrecht, J. 1985. Manganiferous pyroxenes and pyroxenoids from three Pb-Zn-Cu skarn deposits. *Contributions to Mineralogy and Petrology* **89**, 379–93.

Abrecht, J. 1989. Manganiferous phyllosilicate assemblages: occurrences, compositions and phase relations in metamorphosed Mn deposits. *Contributions to Mineralogy and Petrology* **103**, 228–41.

Abrecht, J. & Peters, T. J. 1980. The miscibility gap between rhodonite and bustamite along the join $MnSiO_3$-$Ca_{0.6}Mn_{0.4}SiO_3$. *Contributions to Mineralogy and Petrology* **74**, 261–9.

Ahmad, S. N. & Arthur, W. R. 1980. Fluid inclusions in porphyry and skarn ore at Santa Rita, New Mexico. *Economic Geology* **75**, 229–50.

Baertschi, P. 1976. Absolute ^{18}O content of standard mean ocean water. *Earth and Planetary Science Letters* **31**, 341–4.

Bertelli, M., Baker, T., Cleverley, J. S. & Ulrich, T. 2009. Geochemical modelling of a Zn–Pb skarn: constraints from LA-ICP-MS analysis of fluid inclusions. *Journal of Geochemical Exploration* **102**, 13–26.

Bodnar, R. J. 1993. Revised equation and table for determining the freezing point depression fo H_2O-NaCl solutions. *Geochimica et Cosmochimica Acta* **57**, 683–4.

Bodnar, R. J., Burnham, C. W. & Sterner, S. M. 1985. Synthetic fluid inclusions in natural quartz. III. Determination of phase equilibrium properties in the system H_2O-NaCl to 1000 °C and 1500 bars. *Geochimica et Cosmochimica Acta* **49**, 1861–73.

Bodnar, R. J. & Vityk, M. O. 1994. Interpretation of microthermometric data for H_2O-NaCl fluid inclusions. In *Fluid Inclusions in Minerals: Methods and Applications* (eds B. De Vivo & M. L. Frezzotti), pp. 117–30. Blacksbury, VA: Virginia Technical Institute.

Brown, P. E., Essene, E. J. & Peacor, D. R. 1980. Phase relations inferred from field data for Mn pyroxenes and pyroxenoids. *Contributions to Mineralogy and Petrology* **74**, 417–25.

Cabella, R., Gaggero, L. & Lucchetti, G. 1991. Isothermal isobaric mineral equilibria in braunite-bearing, rhodonite-bearing, johannsenite-bearing, calcite-bearing assemblages from northern Apennine metacherts (Italy). *Lithos* **27**, 149–54.

Canet, C., González-Partida, E., Camprubí, A., Castro-Mora, J., Romero, F. M., Prol-Ledesma, R. M., Linares, C., Romero-Guadarrama, J. & Sánchez-Vargas, L. 2011. The Zn–Pb–Ag skarns of Zacatepec, Northeastern Oaxaca, Mexico: a study of mineral assemblages and ore-forming fluids. *Ore Geology Reviews* **39**, 277–90.

Cang, F. B., Deng, M. G. & Wang, P. 2013. A study on fluid inclusions of Luziyuan Pb-Zn deposit, Zhenkang county, western of Yunnan Province. *Acta Mineralogica Sinica* **S1**, 428–9 (in Chinese with English summary).

Chen, Y. Q., Huang, J. N. & Lu, Y. X. 2009. Geochemistry of elements, sulphur-lead isotopes and fluid inclusions from Jinla Pb-Zn-Ag poly-metallic ore field at the joint area across China and Myanmar border. *Earth Science (Journal of China University of Geosciences)* **34**, 585–94 (in Chinese with English summary).

https://doi.org/10.1017/S001675681700111X Published online by Cambridge University Press

Chen, Y. Q., Lu, Y. X. & Xia, Q. L. 2005. Geochemical characteristics of the Hetaoping Pb-Zn deposit, Baoshan, Yunnan, and its genetic model and ore prospecting model pattern. *Geology in China* **32**, 90–9 (in Chinese with English summary).

Chi, G. X. & Lu, H. Z. 2008. Validation and representation of fluid inclusion microthermometric data using the fluid inclusion assemblage (FIA) concept. *Acta Petrologica Sinica* **24**, 1945–53 (in Chinese with English summary).

Clayton, W. M. & Mayeda, T. K. 1963. The use of bromine penta-fluoride in the extraction of oxygen from oxides and silicates for isotopic analysis. *Geochimica et Cosmochimica Acta* **27**, 43–52.

Coleman, M. L., Sheppard, T. J., Durham, J. J., Rouse, J. E. & Moore, G. R. 1982. Reduction of water with zinc for hydrogen isotope analysis. *Analytical Chemistry* **54**, 993–5.

Craig, H. 1961. Standards for reporting concentrations of deuterium and oxygen 18 in natural waters. *Science* **133**, 1833–4.

De Hoog, J. C. M., Taylor, B. E. & Van Bergen, M. J. 2009. Hydrogen-isotope systematics in degassing basaltic magma and application to Indonesian arc basalts. *Chemical Geology* **266**, 256–66.

Deng, M. G., Li, W. C. & Wen, H. J. 2013. Prospecting significance of rhodonite in the Luziyuan lead-zinc polymetallic ore deposit in Zhenkang, western Yunan. *Geological Bulletin of China* **32**, 1867–9 (in Chinese with English summary).

Dong, W. W. & Chen, S. L. 2007. The characteristics and genesis of Luziyuan Pb-Zn deposit, Zhenkang. *Yunnan Geology* **26**, 404–10 (in Chinese with English summary).

Driesner, T. & Heinrich, C. A. 2007. The system H_2O–NaCl. Part I: correlation formulae for phase relations in temperature–pressure–composition space from 0 to 1000 °C, 0 to 5000 bar, and 0 to 1 XNaCl. *Geochimica et Cosmochimica Acta* **71**, 4880–901.

Einaudi, M. T., Meinert, L. D. & Newberry, R. J. 1981. Skarn deposits. *Economic Geology 75th Anniversary Volume*, 317–91.

Gao, W., Ye, L., Cheng, Z. T. & Yang, Y. L. 2011. Characteristics of isotope geochemistry of Hetaoping Pb-Zn ore in Baoshan,Yunnan Province,China. *Acta Mineralogica Sinica* **31**, 578–86 (in Chinese with English summary).

Giggenbach, W. F. 2003. Magma degassing and mineral deposition in hydrothermal systems along convergent plate boundaries. In *Volcanic, Geothermal and Ore-Forming Fluids: Rulers and Witnesses of Processes within the Earth* (eds S. F. Simmons & I. Graham), pp. 1–18. Society of Economic Geologists Special Publication no. 10.

Goldstein, R. H. & Reynolds, T. J. 1994. *Systematics of Fluid Inclusions in Diagenetic Minerals*. Tulsa, Oklahoma, Society of Economic Paleontologists and Mineralogists. SEPM Short Course no. 31, 199 pp.

González-Partida, E. & Camprubí, A. 2006. Evolution of mineralizing fluids in the Zn–Pb–Cu(–Ag ± Au) skarn and epithermal deposits of the world-class San Martín district, Zacatecas, Mexico. *Journal of Geochemical Exploration* **89**, 138–42.

Han, Y. W. 2010. *A analysis on evolution of ore-forming fluids from the V1 orebody in the Hetaoping skarn Pb-Zn deposit, Baoshan,Yunnan province, SW China*. Master Degree thesis, Kunming University of Science and Technology, Kunmin, China. Published thesis (in Chinese with English summary).

Hoefs, J. 1997. *Stable Isotope Geochemistry*, 4th edn. Berlin and Heidelberg: Springer-Verlag, 201 pp.

Kamvong, T. & Zaw, K. 2009. The origin and evolution of skarn-forming fluids from the Phu Lon deposit, northern Loei Fold Belt, Thailand: evidence from fluid inclusion and sulfur isotope studies. *Journal of Asian Earth Science* **34**, 624–33.

Li, W. C. & Mo, X. X. 2001. The Cenozoic tectonics and metallogenesis in the 'three-river' area of southwest China. *Yunnan Geology* **20**, 333–46 (in Chinese with English summary).

Li, D. X. & Zhao, Y. M. 2004. Skarn mineralization zonation and fluid evolution in the Jiaoli deposit, Jiangxi Province. *Geological Review* **50**, 17–24 (in Chinese with English summary).

Lin, B. X., Deng, M. G., Sha, J. Z. & Liang, X. W. 2013. Discussion on the characteristics of texture and structure of ores and genesis of Luziyuan Pb-Zn-Fe polimetallic deposit in Zhenkang, Yunnan. *Henan Science* **31**, 494–9 (in Chinese with English summary).

Liu, Y. S., Hu, Z. C., Gao, S., Günther, D., Xu, J., Gao, C. G. & Chen, H. H. 2008. In situ analysis of major and trace elements of anhydrous minerals by LA-ICP-MS without applying an internal standard. *Chemical Geology* **257**, 34–43.

Lü, C. L., Deng, M. G. & Hu, W. 2013. Study on metallogenic conditions and occurrence regularity of Luziyuan Pb-Zn deposit, Zhengkang Town, Yunnan Province. *Contributions to Geology and Mineral Resources Research* **28**, 529–34 (in Chinese with English summary).

Megaw, P. K. M., Ruiz, J. & Titley, S. R. 1988. High-temperature, carbonate hosted Ag-Pb-Zn(Cu) deposits of northern Mexico. *Economic Geology* **83**, 1856–85.

Meinert, L. D. 1987. Skarn zonation and fluid evolution in the Groundhog Mine, Central mining district, New Mexico. *Economic Geology* **82**, 523–45.

Meinert, L. D., Dipple, G. M. & Nicolescu, A. S. 2005. World skarn deposits. *Economic Geology 100th Anniversary Volume*, 299–336.

Meinert, L. D., Hedenquist, J. W., Satoh, H. & Matsuhisa, Y. 2003. Formation of anhydrous and hydrous skarn in Cu-Au ore deposits by magmatic fluids. *Economic Geology* **98**, 147–56.

Mo, X. X. & Pan, G. T. 2006. From the Tethys to the formation of the Qinghai-Tibet Plateau:constrained by tectono-magmatic events. *Earth Science Frontiers* **13**, 43–51 (in Chinese with English summary).

Mohapatra, B. K. & Nayak, B. 2005. Petrology of Mn carbonate-silicate rocks from the Gangpur Group, India. *Journal of Asian Earth Science* **25**, 773–80.

Mollai, H., Sharma, R. & Pe-Piper, G. 2009. Copper mineralization around the Ahar batholith, north of Ahar (NW Iran): evidence for fluid evolution and the origin of the skarn ore deposit. *Ore Geology Reviews* **35**, 401–14.

Moura, A. 2008. Metallogenesis at the Neves Corvo VHMS deposit (Portugal): a contribution from the study of fluid inclusions. *Ore Geology Reviews* **34**, 354–68.

Newberry, R. J. 1987. Use of intrusive and calc-silicate compositional data to distinguish contrasting skarn types in the Darwin polymetallic skarn district, California, USA. *Mineralium Deposita* **22**, 207–15.

Ohmoto, H., Kaiser, C. J. & Geer, K. A. 1990. Systematic of sulfur isotopes in recent marine sediments and ancient sediment-hosted base metal deposits. In *Stable Isotope and Fluid Processes in Mineralization, Perth, Australia* (eds. H. K. Herbert & S. E. Ho), pp. 70–120. Geology Department and Extension Service,

https://doi.org/10.1017/S001675681700111X Published online by Cambridge University Press

University of Western Australia, Special Publication no. 23.

Ohmoto, H. & Rye, R. O. 1979. Isotopes of sulfur and carbon. In *Geochemistry of Hydrothermal Ore Deposits* (ed. R. D. Barnes), pp. 509–67. New York: John Wiley and Sons.

Palinkas, S. S., Palinkas, L. A., Renac, C., Spangenberg, J. E., Lueders, V. & Molnar, F. 2013. Metallogenic model of the Trepca Pb-Zn-Ag skarn deposit, Kosovo: evidence from fluid inclusions, rare earth elements, and stable isotope data. *Economic Geology* **108**, 135–62.

Peter, K., Jaroslav, L., Andrew, H. R. & Anthony, E. F. 2004. Fluid evolution in a subvolcanic granodiorite pluton related to Fe and Pb-Zn mineralization, Banska Stiavnica Ore District, Slovakia. *Economic Geology* **99**, 1745–70.

Robinson, B. W. & Kusakabe, M. 1975. Quantitative preparation of sulfur dioxide, for $^{34}S/^{32}S$ analyses, from sulfides by combustion with cuprous oxide. *Analytical Chemistry* **47**, 1179–81.

Roedder, E. 1984. Fluid inclusions. *Reviews in Mineralogy* **12**, 12–26.

Roedder, E. & Bodnar, R. J. 1980. Geologic pressure determinations from fluid inclusion studies. *Annual Review of Earth & Planetary Sciences* **8**, 263–301.

Seghedi, I., Voica Bojar, A., Downes, H., Rosu, E., Tonarini, S. & Mason, P. 2007. Generation of normal and adakite-like calc-alkaline magmas in anonsubductional environment: an Sr-O-H isotopic study of the ApuseniMountains Neogene magmatic province, Romania. *Chemical Geology* **245**, 70–88.

Sheppard, S. 1986. Characterization and isotopic variations in natural waters. *Reviews in Mineralogy and Geochemistry* **16**, 165–83.

Shimizu, M. & Ilyama, J. T. 1982. Zinc-lead skarn deposits of the Nakatatsu mine, central Japan. *Economic Geology* **77**, 1000–12.

Steele-Macinnis, M., Lecumberri-Sanchez, P. & Bodnar, R. J. 2012. Short note: HokieFlincs_H_2O-NaCl: a Microsoft Excel spreadsheet for interpreting microthermometric data from fluid inclusions based on the PVTX properties of H_2O-NaCl. *Computers & Geosciences* **49**, 334–7.

Taylor, H. P. 1997. Oxygen and hydrogen isotope relationships in hydrothermal mineral deposits. *Geochemistry of Hydrothermal Ore Deposits* **3**, 229–302.

Wilkinson, J. J. 2001. Fluid inclusions in hydrothermal ore deposits. *Lithos* **55**, 229–72.

Williams-Jones, A. E., Samson, I. M., Ault, K. M., Gagnon, J. E. & Fryer, B. J. 2010. The genesis of distal zinc skarns: evidence from the Mochito Deposit, Honduras. *Economic Geology* **105**, 1411–40.

Winter, G. A., Essene, E. J. & Peacor, D. R. 1981. Carbonates and pyroxenoids from the manganese deposit near Bald Knob, North Carolina. *American Mineralogist* **66**, 278–89.

Xia, Q. L., Chen, Y. Q. & Lu, Y. X. 2005. Geochemistry, fluid inclusion, and stable isotope studies of Luziyuan Pb-Zn Deposit in Yunnan Province, southwestern China. *Earth Science (Journal of China University of Geosciences)* **30**, 177–86 (in Chinese with English summary).

Xu, Q. & Mo, X. 2000. Regional fluid characters and regimes of 'Sanjiang' middle belt during Neo-Tethys. *Acta Petrologica Sinica* **16**, 639–48 (in Chinese with English summary).

Xue, C. D., Han, Y. W., Huang, Q. H., Li, J. & Dong, X. G. 2011. Genesis and mineragenetic epoch of the Hetaoping Pb-Zn deposit in Baoshan area, Yunnan: a remote skarn-hydrothermal deposit. *Acta Mineralogica Sinica* **S1**, 415–18 (in Chinese with English summary).

Xue, C. D., Han, R. S. & Yang, H. L. 2008. Isotope geochemical evidence for ore-forming fluid resources in Hetaoping Pb-Zn deposit, Baoshan, northwestern Yunnan. *Mineral Deposits* **27**, 243–52 (in Chinese with English summary).

Yang, X. F. & Luo, G. 2011. A tentative analysis of the ore-controlling factors of the Luziyuan lead-zinc deposit in Zhenkang area,Yunnan. *Geological Bulletin of China* **30**, 1137–46 (in Chinese with English summary).

Yang, Y. L. 2013. *A geochemical study on the Luziyuan skarn type Pb-Zn deposit in the Baoshan terrane, Yunnan,China*. Master Degree thesis, Institute of Geochemistry, Chinese Academy of Sciences, Guiyang, China. Published thesis (in Chinese with English summary).

Yang, Y. L., Ye, L., Cheng, Z. T. & Bao, T. 2013. Origin of fluids in the Hetaoping Pb-Zn deposit, Baoshan-Narong-Dongzhi block metallogenic belt, Yunnan Province, SW China. *Journal of Asian Earth Science* **73**, 362–71.

Yang, Y. L., Ye, L., Cheng, Z. T., Bao, T. & Gao, W. 2012. A tentative discussion on the genesis of skarn Pb-Zn deposits in the Baoshan-Zhenkang terrane. *Acta Petrologica et Mineralogica* **31**, 554–64 (in Chinese with English summary).

Ye, L., Bao, T. & Yang, Y. L. 2013. A discussion on geochemistry of Luziyuan Pb-Zn ploymetallic ore deposit, Zhenkang county, in the Bao-Shan terrane. *Acta Mineralogica Sinica* **S1**, 531 (in Chinese with English summary).

Ye, L., Cook, N. J., Ciobanu, C. L., Liu, Y. P., Zhang, Q., Liu, T. G., Gao, W., Yang, Y. L. & Danyushevskiy, L. 2011*a*. Trace and minor elements in sphalerite from base metal deposits in South China:a LA-ICPMS study. *Ore Geology Reviews* **39**, 188–217.

Ye, L., Gao, W., Cheng, Z. T., Yang, Y. L. & Tao, Y. 2010. LA-ICP-MS zircon U-Pb geochronology and petrology of the Muchang Alkali Granite, Zhenkang County, Western Yunnan Province, China. *Acta Geologica Sinica – English Edition* **84**, 1488–99.

Ye, L., Yang, Y. L. & Bao, T. 2011*b*. A preliminary study on metallogenesis of Hetaoping and Luziyuan skarn Pb-Zn deposit in the Baoshan terrane, Yunnan province. *Acta Mineralogica Sinica* **S1**, 659 (in Chinese with English summary).

Yun, S. & Einaudi, M. T. 1982. Zinc-lead skarns of the Yeonhwa-Ulchin district, South Korea. *Economic Geology* **77**, 1013–32.

Zhao, Y. M., Dong, Y. G., Li, D. X. & Bi, C. S. 2003. Geology, mineralogy, geochemistry, and zonation of the Bajiazi dolostone-hosted Zn–Pb–Ag skarn deposit, Liaoning Province, China. *Ore Geology Reviews* **223**,153–82.

Zhao, Z. F., Lu, Y. X. & Xie, Y. H. 2002. An example study of remote sensing and Gis metallogenetic prognosis in Luziyuan area, Zhenkang. *Yunnan Geology* **21**, 300–7 (in Chinese with English summary).

Zheng, Y. F. 1993. Calculation of oxygen isotope fractionation in anhydrous silicate minerals. *Geochimica et Cosmochimica Acta* **57**, 1079–91.

Zhu, Y. Y., Han, R. S. & Xue, C. D. 2006. Geological character of the Hetaoping lead zinc deposit of Baoshan,Yunnan province. *Mineral Resources and Geology* **20**, 32–5 (in Chinese with English summary).

https://doi.org/10.1017/S001675681700111X Published online by Cambridge University Press